LITHOS 456-457 (2023) 107275

Contents lists available at ScienceDirect

LITHOS

journal homepage: www.elsevier.com/locate/lithos

The B isotopic signature of serpentine from obducted ophiolites: Mixing of fluids and tectonic implications

Celine Martin [a,*], Kennet E. Flores [b,a], George E. Harlow [a], Samuel Angiboust [c], Florent Hodel [d], George L. Guice [a]

[a] Department of Earth and Planetary Sciences, American Museum of Natural History, New York, NY 10024-5192, USA
[b] Department of Earth, Marine and Environmental Sciences, University of North Carolina, Chapel Hill, NC 27599-3315, USA
[c] Ecole Normale Supérieure de Lyon, Université Lyon 1, CNRS, F-69007 Lyon, France
[d] Laboratoire Chrono-Environnement, UMR6249 CNRS-UFC, Besançon, France

ARTICLE INFO

Keywords:
Obducted ophiolites
Supra Subduction Zone ophiolites
B isotopic signatures
Serpentinites
Mixing of fluids

ABSTRACT

Obducted ophiolites expose oceanic lithosphere slivers in suture zones. The few previous studies focusing specifically on the serpentinization of the ultramafic part of ophiolites mostly concluded that serpentinization was driven by seawater. Recent developments in B isotope geochemistry have enabled the tracking of fluid source(s) in serpentinites, suggesting $\delta^{11}B$ values above +10‰ mostly reflect seawater hydration and $\delta^{11}B$ values below +10‰ mostly reflect hydration by subducted crust-derived metamorphic fluids. In this study, we further investigate the fluid sources recorded by ophiolitic serpentinites by presenting B isotopic geochemistry for seventeen samples from well-characterized ophiolites in Guatemala, Iran, and Brazil. The samples from Guatemala and Iran are from fossil Supra Subduction Zones (SSZ), while samples from Brazil represent a fossil Ocean-Continent Transition (OCT). Most of the samples display the pseudomorphic mesh matrix and bastite microtexture typical of serpentinites. Nine of the samples are either totally (both microtextures) or partially (one microtexture only) out of isotopic equilibrium, with $\delta^{11}B$ variations of up to 18‰ within individual samples/textures. Among the samples with a narrow $\delta^{11}B$ range (i.e., at isotopic equilibrium), those from a fossil OCT ophiolite have $\delta^{11}B$ ranging from +3.8 to +23.2‰, which is broadly consistent with serpentinization by seawater. In contrast, serpentinites from fossil SSZ ophiolite have $\delta^{11}B$ straddling 0‰, ranging from −7.7 to +13.5‰. These data indicate that seawater alone cannot be responsible for serpentinization of these ultramafic rocks, but rather either subducted crust-derived metamorphic fluids, or a mixture of seawater and subducted crust-derived metamorphic fluids. This interpretation agrees with the recent suggestions that SSZ ophiolites possibly represent fossil forearc lithosphere.

1. Introduction

The term obducted ophiolite was originally coined to describe a part of a fossil oceanic lithosphere thrusted onto the continental crust margin (Steinmann, 1927). The oceanic material is interpreted as having been produced at mid-ocean ridges and then "trapped" during the closure of ocean basins. From the initial definition, ophiolites contain, from the top to the bottom: volcanic rocks (pillow basalt), sheeted dikes, gabbros, cumulates, and upper mantle rocks (Penrose Conference, 1972). However, several early publications pointed out that the volcanic rocks at the top of ophiolitic complexes present geochemical similarities with the arc-related lavas produced at convergent margins (Miyashiro, 1973; Pearce et al., 1984). These ophiolites, containing arc-like lavas, were termed suprasubduction zone (SSZ) ophiolites, in reference to the seemingly paradoxical chemical affiliation with subduction zones (Pearce et al., 1984; Pearce and Reagan, 2019). This observation was initially explained by a hypothesis whereby SSZ ophiolites form in association with island arcs (extensional systems associated with convergent margins), reconciling the geochemical evidence with structural evidence for seafloor spreading (Dewey, 1976; Pubellier et al., 2004). More recently, SSZ ophiolites have been interpreted as representing ancient forearc lithosphere (e.g., Stern et al., 2012), by comparison with studies focusing on the present-day Izu-Bonin Mariana trench system (e.g., Ishizuka et al., 2010, 2006). Forearc lithosphere is indeed optimally

* Corresponding author.
E-mail address: cmartin@amnh.org (C. Martin).

https://doi.org/10.1016/j.lithos.2023.107275
Received 27 January 2023; Received in revised form 23 June 2023; Accepted 3 July 2023
Available online 6 July 2023

situated for obduction and associated preservation as ophiolites (Casey and Dewey, 1984; Metcalf and Shervais, 2008; Wakabayashi and Dilek, 2004): it comprises young, hot, and buoyant material, which prevents its subduction but facilitates ophiolite obduction (Stern et al., 2012). Several publications additionally suggest that the formation of ophiolites is related to incipient subduction (e.g., Moores, 1982; Pearce et al., 1984; Prigent et al., 2018). The obduction of ophiolites is then facilitated by a metamorphic sole, usually amphibolite, representing the metamorphosed oceanic crust subducting below ophiolite (e.g., Moores, 1982; Prigent et al., 2018; Wakabayashi and Dilek, 2004). Regardless of the tectonic setting (spreading center, back-arc, or forearc) in which the future ophiolite forms, all authors agree that an ophiolite represents a sliver of the oceanic upper plate (i.e., not the subducting plate). Thus, the meta-ophiolite complexes (e.g., Western Alps and other low temperature – high pressure metamorphic belts) will not be considered here, as they represent parts of subducted slabs (e.g., Barnicoat and Cartwright, 1995; Ernst and Dal Piaz, 1978).

The lowermost part of ophiolites represents the upper mantle and is partly or totally serpentinized. However, little is known about the origin of the fluid(s) responsible for its serpentinization. It is commonly accepted that ophiolites (irrespective of the layer considered) are altered by seawater, because they represent slivers of oceanic crust, and consequently have been – at least to some extent – in contact with seawater during seafloor residency (e.g., Gregory, 2003; Mcculloch et al., 1980). There has been limited research focusing on the serpentinization of obducted ophiolites, including the nature of fluid(s) responsible for serpentinization. Most studies have concluded that seawater was responsible for serpentinization, whether on the basis of trace elements (Agranier et al., 2007; Li and Lee, 2006) or B isotopes (Lécuyer et al., 2002; Martin et al., 2016). However, Prigent et al. (2018) recently suggested that the fluids responsible for serpentinization of the mantellic part are metamorphism-related fluids, on the basis on B isotopes. Boron isotopes have indeed been used for tracking the source of fluids encountered in subduction zones (e.g., Angiboust et al., 2014; Harvey et al., 2014a; Martin et al., 2016, 2020; Scambelluri and Tonarini, 2012; Yamada et al., 2019b, 2019a). Martin et al. (2020) suggested that serpentinites showing a $\delta^{11}B$ above +10‰ represent a mantle hydrated by seawater-derived fluid, whereas serpentinites showing a $\delta^{11}B$ below +10‰ have mostly been hydrated by subducted crust-derived metamorphic fluids. However, a slight overlap of both fluids (seawater and subducted crust-derived metamorphic fluids) is visible for serpentinite with $\delta^{11}B$ in the range +5 to +10‰, meaning values in this range may not allow concluding for the origin of the fluid responsible for serpentinization. In the present paper, serpentinites from well-characterized SSZ ophiolites located in the Guatemala Suture Zone (Guatemala; seven samples) and in the Sistan Suture Zone (Iran; two samples) have been selected and their B contents and isotopic signatures acquired to determine the source of fluid(s) responsible for serpentinization in obducted ophiolites. Eight samples from the Araguaia Belt (Brazil), which represent serpentinites from a passive margin Ocean-Continent Transition (OCT, as defined by Picazo et al. (2016)), have also been studied to compare their B isotopic signatures with those of SSZ ophiolites.

2. Geological background of the studied samples

2.1. Guatemala

The Cretaceous Guatemala Suture Zone (GSZ) is the fault-bound region in central Guatemala that contains the present North American–Caribbean plate boundary, the left-lateral, strike-slip Motagua fault system (Flores et al., 2013). The GSZ is bounded north and south by two continental crust blocks (Maya and Chortís, respectively) and contains various high-grade schist and gneisses, accreted metavolcanic-metasedimentary sequences, low-grade schists and metasediments, serpentinite mélanges and obducted ophiolites. The complex tectonic assemblages contain the relics of Pacific-type subduction margin (i.e., south GSZ) and the closure of proto-Caribbean back arc basin (i.e., north GSZ; Flores et al., 2015, 2013). The serpentinite mélanges occur north and south of the Motagua fault system and enclose high-pressure–low-temperature (HP–LT) rocks such as eclogite, jadeitite, garnet-amphibolite, and blueschist (Brueckner et al., 2009; Harlow et al., 2004; Tsujimori et al., 2006). Based on the association of a serpentinite matrix, HP–LT blocks, and vein-related metamorphic rocks, these mélanges have been interpreted as examples of subduction channel (deep mantle wedge) sequences exhumed from depths up to 80–100 km (Flores et al., 2013; Martin et al., 2020, 2016). The main bodies of dismembered ophiolite sequences (Baja Verapaz and Sierra de Santa Cruz) are found in the northern section of the GSZ, where they have been thrust over the passive margin sedimentary sequences of the Maya block (Fig. 1a). Smaller ophiolitic slivers (e.g., Juan de Paz) also occur north and south of the Motagua fault system, tectonically associated with various metamorphic sequences and serpentinite mélanges (Flores et al., 2013).

The samples MVE15-9-2 and MVE15-9-5 were collected ~3 km north of the Motagua fault in the eastern section of the Guatemala Suture Zone near Concua (Fig. 1a). This area consists of a tectonic association of slivers of high-grade metamorphic rocks and serpentinite mélanges of the Chuacus complex and North Motagua Mélange, respectively (Flores et al., 2013). Samples from this locality occur within a km-sized sliver composed of stacks of serpentinites containing rodingites, metabasalts, low-grade metasediments, and partially metamorphosed limestones. This sequence resembles the associations of the Juan de Paz and Sierra de Santa Cruz ophiolites. The MVE10-10-1 serpentinite sample is taken from sliver of ultramafic rocks that is a hundred meters long, in tectonic association with metabasalts, and that outcrops parallel to the western Motagua fault system near the town of Gualan (Fig. 1a). This ophiolitic sliver overthrusts the low-medium grade metasediments of the Las Ovejas Complex from the south GSZ (Flores et al., 2013). Samples from the MVE15-17 locality were collected in the southern region of the GSZ near Potrero Carrillo, ~14 km south of the Motagua fault system (Fig. 1a). This area consists of a southward imbricated stack of tectonic slivers composed of serpentinite mélanges, low-medium grade metavolcanic-metasedimentary sequences, and massive ultramafic slivers (e.g., Potrero Carrillo) grouped as South Motagua Mélange and El Tambor complex, respectively (Flores et al., 2013). The Potrero Carrillo sliver (El Tambor complex) is a massive, partially serpentinized body; no association with metasediments, metabasalts, or HP-LT rocks was observed.

2.2. Iran

The Sistan ophiolitic Suture Zone, now exposed along the Iran-Afghanistan border, comprises a paleo-accretionary wedge formed by the closure of the Sistan Ocean, a N-S extension of the Neotethys, during late Cretaceous times (99.6 Ma - 65.5 Ma; e.g., Angiboust et al., 2013; Bonnet et al., 2018; Tirrul et al., 1983). This wedge consists of three distinct units with markedly different metamorphic imprints. Some dismembered eclogites are preserved as blocks and lenses in a weak matrix (the "eclogitic unit") overlain by large coherent masses of epidote blueschist-facies metasediments (Angiboust et al., 2013; Bonnet et al., 2018; Fotoohi Rad et al., 2005). This High Pressure-Low Temperature material is commonly (tectonically) overlain by obducted, coherent, laterally-continuous slivers that comprise weakly-deformed serpentinized ultramafics associated with red radiolarian cherts, basalts or gabbros, and various folded flysch and tuff sequences (e.g., Babazadeh and De Wever, 2004; Delaloye and Desmons, 1980; Tirrul et al., 1983). The unit has been referred as the "Western Unit" in a field study by Angiboust et al. (2013), and samples Su09-17 and m52 are from this unit (see sample location in Fig. 1b)

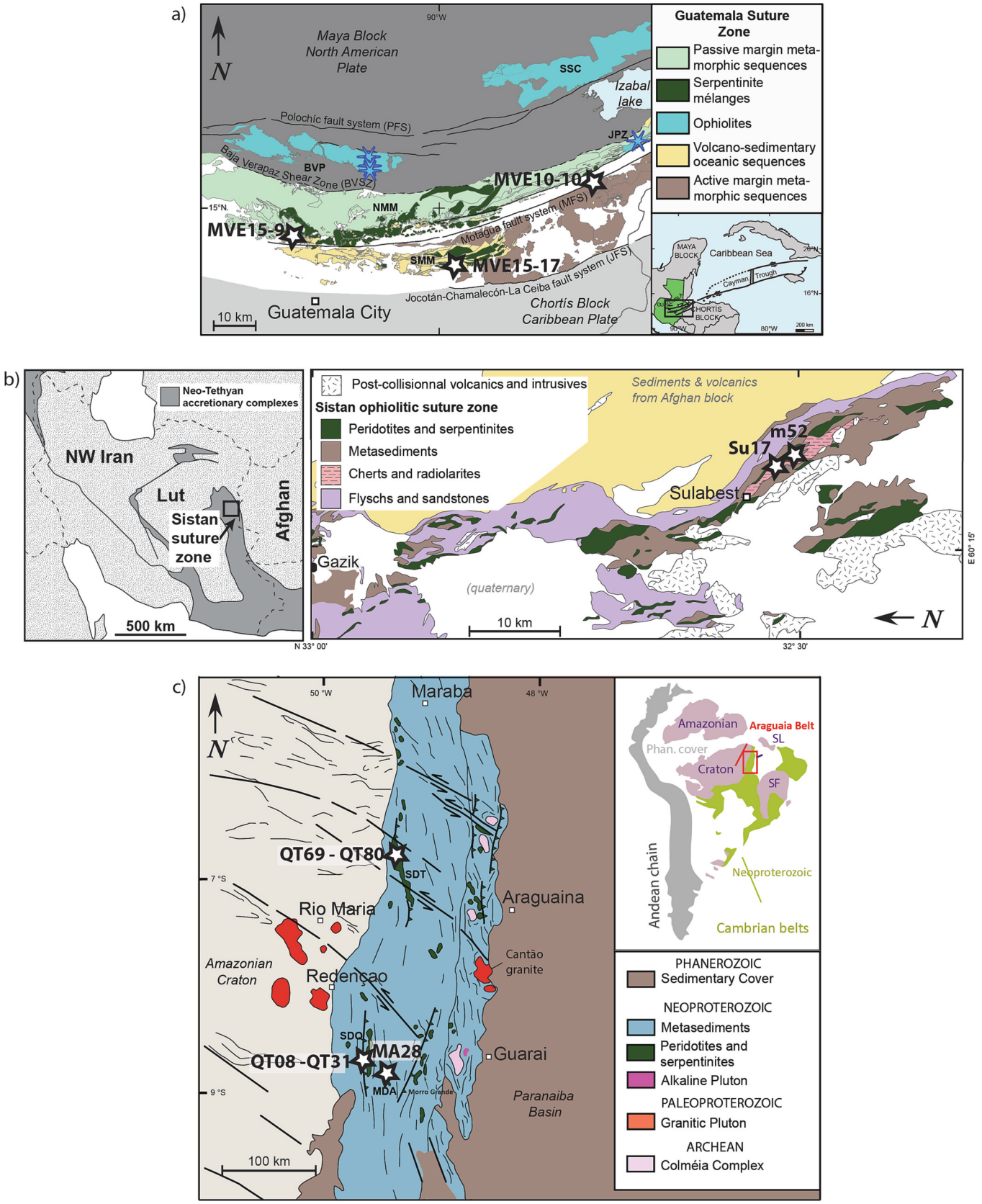

Fig. 1. Geological maps of the studied areas. a), Guatemala Suture Zone, Guatemala (after Flores et al., 2013), b) Sistan ophiolitic suture zone, Iran (after Angiboust et al., 2013), and c) Araguaia Belt, Brazil (after Hodel et al., 2019). The white stars represent the location of the samples studied in the present paper. The blue stars on a) represent the samples published in Martin et al. (2016) and added in the discussion on the present paper. (For interpretation of the references to colour in this figure legend, the reader is referred to the web version of this article.)

2.3. Brazil

The Araguaia Belt is a 1200 km long and 150 km wide Neoproterozoic fold and thrust belt located in central Brazil. Bordering the eastern Amazonia Craton, it results from the collision between the Parnaíba block and the Amazonian, the West African and the São Francisco-Congo cratons during the Panafrican/Brasiliano orogeny (e.g., Daly et al., 2014; Hodel et al., 2019; Moura and Gaudette, 1993). It mainly consists in low-grade metasedimentary rocks (Estrondo and Tocantins Groups, Hasui et al., 1977) in which mafic/ultramafic bodies outcrop (dismembered ophiolitic units, Alvarenga et al., 2000; Gorayeb, 1989; Hodel et al., 2019; Paixão et al., 2008). Recently, Hodel et al. (2019) proposed that the Araguaia Belt constitutes the remnants of a Neoproterozoic ocean-continent transition (OCT, passive margin). Serpentinite samples of the present study originate from the two main ultramafic complexes of the Araguaia Belt: the Serra do Quatipuru unit (QT-08 to QT-31), and the Serra do Tapa unit (QT-69 to QT-80) (Fig. 1c).

3. Methods

Serpentinite polysomes from Guatemala have been identified using X-ray diffraction on 1-in. diameter polished sections (Rigaku DMAX/RAPID instrument, with JADE (MDI) software and the International Center for Diffraction Data PDF-2 database for phase identification, AMNH). Additionally, one sample (MVE15-17-3) has been analyzed as a demonstration of a new Raman Integrated Scanning Electron Microscope (RISE). The serpentinite polysomes of samples from Iran and Brazil have been identified by Raman spectroscopy (respectively Angiboust et al., 2013, and Hodel et al., 2019).

Trace element contents were analyzed in situ by LA-ICP-MS with an ESI New Wave UP-193-FX ArF* (193 nm) excimer laser coupled to a VG PQ ExCell (ThermoScientific) ICP-MS at Lamont Doherty Earth Observatory, Columbia University and a Photon Machine (193 nm) excimer laser coupled to an ICap QC (ThermoScientific) ICP-MS at the Department of Earth and Planetary Sciences, Rutgers University. The following isotopes were monitored: ^{7}Li, ^{11}B, ^{24}Mg, ^{29}Si, ^{52}Cr, ^{55}Mn, ^{57}Fe, ^{59}Co, ^{60}Ni, ^{63}Cu, ^{66}Zn, ^{75}As, ^{85}Rb, ^{88}Sr, ^{90}Zr, ^{121}Sb, ^{133}Cs, ^{137}Ba, ^{139}La, ^{140}Ce, ^{141}Pr, ^{145}Nd, ^{147}Sm, ^{153}Eu, ^{157}Gd, ^{159}Tb, ^{163}Dy, ^{165}Ho, ^{166}Er, ^{169}Tm, ^{172}Yb, ^{175}Lu, and ^{178}Hf. Analyses were performed using traverses (~200 μm long, with a beam diameter of 100 μm (LDEO) and 85 μm (Rutgers University)) at a repetition rate of 10 Hz and a monitored energy density of 10 J/cm^2 on the sample surface. Using ^{29}Si as an internal standard, quantification was performed via external calibration using several glass reference materials (U.S. Geological Survey natural glasses BHVO-2G, BIR-1G and BCR-2), and these same standards were run as unknown material to validate the measurements. Based on the standards and settings described, external reproducibility for the elements measured was typically below 10–15% relative standard deviation (Supplementary Material 1, Table SM1).

Boron isotopes from Guatemalan and Iranian samples were measured in situ by LA-MC-ICP-MS, using an ESI New Wave UP-193-FX ArF* (193 nm) excimer laser coupled to a Neptune Plus (ThermoScientific) MC-ICP-MS (Lamont Doherty Earth Observatory, Columbia University), following the method developed by Martin et al. (2015). The instrument was setup with Ni / Jet X cones and a RF power of 1100 W. The data were collected by electron multipliers with a repetition rate of 10 Hz, at a speed of 3 μm per second, along traverses of ~300 μm in length and between 75 and 175 μm in diameter. Brazilian serpentinites were measured using a Photon Machine (193 nm) excimer laser coupled to a Neptune Plus (ThermoScientific) MC-ICP-MS (Department of Earth and Planetary Sciences, Rutgers University), with a repetition rate of 10 Hz and a fluence of ~5 J/cm^2 on the sample surface, along traverses of ~600 μm in length and 40 μm in diameter. The isotopes have been collected by electron multiplier for ^{10}B, and Faraday cup (with a 10^{12} Ω amplifier) for ^{11}B. Boron isotopic data on sample Q80 (Brazil) have been collected using both instruments (see Martin et al., 2020 for a detailed comparison of the data acquired on both instruments). Mass-bias correction was performed with the standard-bracketing method, using NIST SRM 612 standard glass (see Martin et al., 2015 for details), and the variations in B intensity are corrected following the calibration method also described in Martin et al. (2015). The B isotopes results are presented using δ notation (see formula below), in which $^{11}B/^{10}B_{sample}$ is the isotopic ratio measured on the sample, and $^{11}B/^{10}B_{standard}$ the isotopic ratio of the reference material SRM 951 (Catanzaro, 1970, U.S. National Institute of Standards and Technology, NIST). The error given for each result (samples, standards, and standards used for bracketing) has been propagated from the error (2 S.E.) on the measured $^{11}B/^{10}B$ and the published error on the standard SRM 951 ($^{11}B/^{10}B = 4.044 \pm 0.001$, Catanzaro, 1970)

$$\delta^{11}B = \left(\frac{\left({}^{11}B/{}^{10}B \right)_{sample}}{\left({}^{11}B/{}^{10}B \right)_{standard}} - 1 \right) \times 1000$$

The standard used to monitor and bracket the B isotopes measurements by LA-MC-ICP-MS is NIST SRM 612 ($^{11}B/^{10}B = 4.048$, Jochum and Stoll (2008), compiled value). It yields $\delta^{11}B$ of +0.72 ± 2.49‰ (2 S.D., $n = 171$), using Lamont Doherty Earth Observatory instrument, and of +0.53 ± 2.09‰ (2 S.D., $n = 42$), using Rutgers University instrument, in agreement with previously published values of +0.68 ± 3.31‰ (2 S.D., Martin et al., 2015) and − 0.51 ± 0.52‰ (Kimura et al., 2016), both using the same analytical in situ method. This value is also consistent with the wet chemistry values ranging from −1.07 ± 0.85‰ (minimum value, Kasemann et al. (2001)) to +0.10 ± 0.40‰ (maximum value, Jochum et al. (2011)). The synthetic glass NIST SRM 610 has been run as unknown and yield $\delta^{11}B$ of +0.97 ± 3.43‰ (2 S.D., $n = 11$) using LDEO instrument, in agreement with the published in situ values of −0.27 ± 2.88‰ (2 S.D., Martin et al., 2015) and −0.33 ± 0.28‰ (Kimura et al., 2016). This value is also in agreement with the wet chemistry values ranging from −1.31 ± 0.68‰ (minimum value, Kasemann et al. (2001)) to 0.00 ± 0.20‰ (maximum value, Jochum et al. (2011)). The serpentinite standard UB-N has been measured in a separate session using LDEO instrument, and the preliminary results yield $\delta^{11}B$ of +9.24 ± 1.92‰ (2 S.D., $n = 5$). This result is in agreement with the two previously published wet chemistry values of +10.47 ± 0.26‰ (1 S.D., Zhu et al., 2021) and + 13.1 ± 0.3‰ (2 S.D., Gangjian et al., 2013). These results indicate that possible matrix effects due to the difference of chemical composition between standards (synthetic glasses) and serpentine minerals are likely negligeable, as expected by Yamada et al. (2019a), who estimated the matrix effect in the range of ±0.5‰. Additionally, the fact that NIST SRM 612 (~35 ppm), UB-N (~140 ppm), and NIST SRM 610 (~350 ppm) gave accurate isotopic values indicate that there is no significant impact of the B content on the measured isotopic value.

4. Samples and petrographic description

Sample MVE15-9-2 (Concua, Guatemala) is a dark green massive serpentinite made of lizardite with magnetite and calcite as accessory phases (Table 1). No relicts of mantellic phases or bastite textures are visible (Fig. 2a). MVE15-9-5 (Concua, Guatemala) is a dark green sample cut by folded veins of diopside (Fig. 2b), with some bastite visible in thin section (Fig. SM2-1a, 1b). The serpentine polysomes are lizardite and antigorite in the bastite, likely lizardite, antigorite + chrysotile in the matrix (Table 1), and nodules of Cr-rich spinel are present as an accessory phase (Fig. 2b; Table SM2). In both samples, the structural formulae show that matrix serpentine have Si content higher than pure lizardite or chrysotile (on average 2.03–2.04 apfu, Table SM2, while Si in pure lizardite/chrysotile is ~2 apfu), likely indicating interlayers of talc in the serpentine crystals.

Sample MVE10-10-1 (Gualan, Guatemala) is a massive, light green

Table 1
Serpentinite samples mineralogy (abbreviations from Whitney and Evans, 2010).

Sample	atg	ctl	lz	tlc	chl	spinel	ol	px	opl	Vein
North GSZ										
MVE15-9-2			+			+				None
MVE15-9-5	+		+			+				di
South GSZ										
MVE10-10-1		+	+							clc + lz
MVE15-17-1b		+	+	+	+	+			+	opl + tlc + srp
MVE15-17-2			+			+				None
MVE15-17-3	+	+	+			+				atg
MVE15-17-4		+	+			+			+	lz/atg?
Sulabest										
Su09-17		+	+				+	+		None
m52		+	+			+				None
Araguaia Belt										
QT08	+	+	+							
QT09	+	+	+							
QT31	+	+	+							
MA28	+	+	+							
QT69	+		+							atg
QT78	+		+							atg
QT79	+		+							atg
QT80	+		+							atg

serpentinite, with some bastite. Both microtextures consist of lizardite + chrysotile (Table 1), and as with samples MVE15-9, the higher contents of Si apfu in the matrix (Table SM2) may indicate interlayers of talc in the serpentine crystals. A vein made of a mixture of lizardite and calcite cut the sample (Fig. 2c).

Samples from Potrero Carillo, Guatemala (MVE15-17-1b, MVE15-17-2, MVE15-17-3, and MVE15-17-4) are medium green serpentinites consisting of lizardite, chrysotile, and minor antigorite. Except MVE15-17-2, which has the typical mesh matrix and bastite texture visible in thin section (Fig. SM2-1g, 1h), the samples display white and green patches, both made of lizardite and chrysotile mixture (Fig. 2d, e, f, Fig. SM2-2a) that are indistinguishable under the microscope (Fig. SM2-1c, 1d) or in BSE (Fig. SM2-2b). As with the other samples from Guatemala, the Si content of these serpentine polysomes is significantly higher (~2.03 to 2.05 apfu) than typical lizardite or chrysotile (~2.00 apfu), probably indicating interlayering with talc (Table SM2). Sample MVE15-17-1b also contains some chlorite (clinochlore) in the green matrix and the white patches, chromite as an accessory phase, and orange areas that are made of a mix of serpentine (lizardite and chrysotile) and probably opal, talc, and Fe, Ni-rich spinel (Table SM2). The orange coloring may be due to meteoric alteration of the spinel, or to oxidation of sulfide. A vein of opal, with minor amounts of talc and serpentine, crosscuts the sample (Fig. 2d, Fig. SM2-1e, 1f, and Table SM2). The serpentine and chlorite chemistry are similar in both the green and white areas (Table SM2). Sample MVE15-17-2 has a simple mineralogy, made of lizardite only, in both the matrix and bastite. The accessory phase is Cr-rich spinel with magnetite overgrowths (Fig. 2e; Table SM2). Samples MVE15-17-3 and MVE15-17-4 also have green and white patches made of lizardite and chrysotile for the green ones, slightly enriched in Cr_2O_3, and lizardite ± talc for the white patches. MVE15-17-3 has spinel, magnesioferrite, magnesiochromite, and magnetite as accessory phases (Table SM2), with talc at the core of the white patches, and some antigorite veinlets have been identified using the RISE system (Fig. SM2-2). MVE15-17-4 is cut by a vein of lizardite and/or antigorite, and displays opal grains, which are also present in the opaque nodules, together with magnetite (Fig. 2f; Table SM2).

Sample Su09-17 and m52 from the Sulabest region (Sistan ophiolitic belt, Iran, Fig. 1b) are massive lizardite-bearing serpentinites with minor chrysotile (Table 1, Angiboust et al., 2013). Su09-17 exhibits two pyroxenes (enstatite and diopside) and olivine (Fo_{90}) (Table SM2). Sample m52 contains bastite (lizardite) and magnesioferrite as accessory phase.

Samples from the Araguaia Belt (Brazil) have been previously described (Hodel et al., 2019). They all display the typical pseudomorphic mesh and bastite texture. The serpentine polysomes present in samples from Serra do Quatipuru (QT08, QT09, and QT31) and samples from Morro do Agostinho (MA28) are mostly lizardite and chrysotile, with minor antigorite, while samples from Serra do Tapa (QT69, QT78, QT79, and QT80) are characterized by a mesh matrix made of a mixture of lizardite and antigorite, cut by antigorite veins.

5. Results

5.1. Trace element contents of serpentinites

5.1.1. In SSZ ophiolites

At Concua (Guatemala), the Fluid Mobile Elements (FME = Li, B, As, Sb, Cs) contents of sample MVE15-9-2 – which displays a homogeneous texture with no relict of mantellic minerals or bastite – are above detection limits (except for As). By contrast, in sample MVE15-9-5, the FME contents are mostly below detection limits with the exception of B and Li, which have similar concentrations in the matrix and the bastite, and slightly lower than in MVE15-9-2 (Fig. 3, Table SM1). Siderophile elements display some differences related to the microtextures of serpentine in MVE15-9-5 (Fig. 3): Ni is slightly enriched in the matrix compared to the bastite, while Cr shows the opposite, in broad agreement with EMPA results (Table SM2). Interestingly, the Ni content of this sample is one order of magnitude lower than MVE15-9-2 (same outcrop), and overall, significantly lower than any of the studied samples (Fig. 3, Table SM1). This likely indicate that Ni was leached by the fluid responsible for the formation of the diopside vein, while Sr was brought by that same fluid.

In sample MVE10-10-1, from Gualan (Guatemala), the serpentine is present in three microtextures: matrix, bastite, and in a vein where it is mixed with calcite, and each of these microtextures shows significant difference in FME. Lithium is enriched in the bastite in comparison to the matrix, while B shows the opposite, and the vein has the lowest contents for both elements (Table SM1). Arsenic shows similar concentrations,

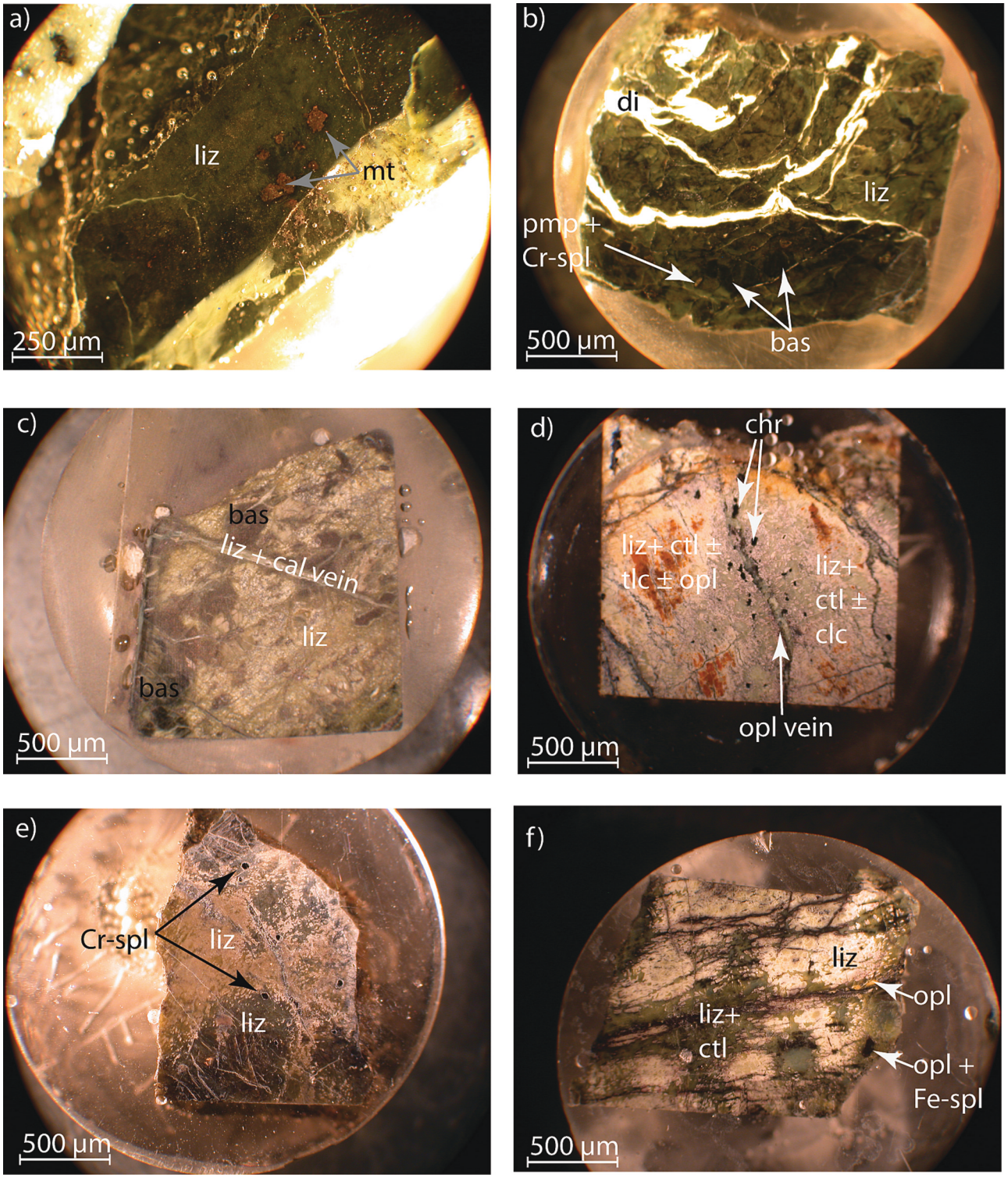

Fig. 2. Selection of 1-in. round polished section representative of samples from Guatemala (northern a, b, c; southern d, e, f). a) sample MVE15-9-2, showing massive lizardite (liz) and magnetite (mt) as accessory phase, b) sample MVE15-9-5, collected on the same outcrop as a), showing some bastite (bas) in a lizardite matrix cut by folded veins of diopside (di), c) sample MVE10-10-1, showing the classic mesh and bastite texture cut by a vein of lizardite and calcite, d) sample MVE15-17-1b showing pale green, white, and orange patches cut by a vein of opal displaying chromite at its edges, e) sample MVE15-17-2 showing the classic mesh and bastite texture, and f) MVE15-17-4, showing the unusual green and white patches, mineralogically similar. (For interpretation of the references to colour in this figure legend, the reader is referred to the web version of this article.)

within error, in the three microtextures (Table SM1). Chromium is enriched in the bastite in comparison to the matrix, and Ni has similar concentrations, within error, in both matrix and bastite (Table SM1). Only two points were measured within the vein, yielding inconclusive results for Cr. Nickel abundance is lower in the vein than in the host material, although the results overlap within error (Table SM1).

Samples from Potrero Carrillo (Guatemala) mostly contain green and white patches, respectively made of lizardite and chrysotile, some with

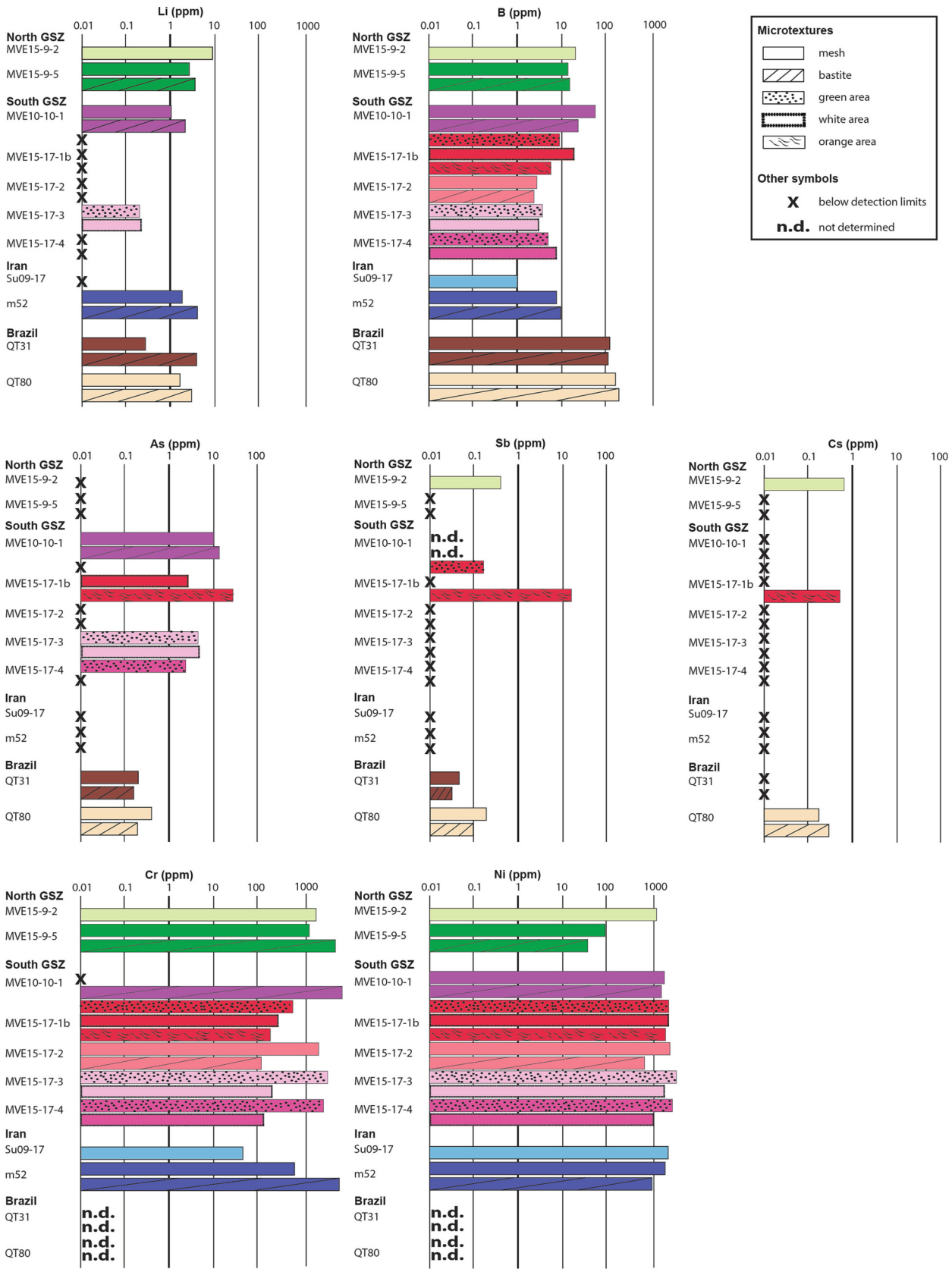

Fig. 3. FME and transition metal (Cr, Ni) contents of the different microtextures of serpentine of the studied samples (logarithmic scale).

accessory chlorite (MVE15-17-1b). The trace elements have been measured in situ in the different microtextures of serpentine. Sample MVE15-17-1b shows differences in function of the serpentine microtextures. The FME concentrations in the green areas are below the detection limits, except for B, while As and B contents are measurable in the white areas (Fig. 3, Table SM1). Nickel and Cr have equivalent concentrations, within error, between both areas (Table SM1). The orange areas, which are a mixture of lizardite, chrysotile, opal, talc, and Fe-Ni-rich spinel are higher in FME, except B, and lower for Cr and Ni (Fig. 3). However, the silica content used for normalization in the LA-ICP-MS analyses has been set as the average of EMPA results acquired in these areas and is therefore imprecise (Table SM2). The values reported above and in Table SM1 for the orange areas are consequently estimates. In MVE15-17-2, except for B, the FME concentrations are systematically below detection limits in both the matrix and bastite (Fig. 3, Table SM1). Boron is the same in the matrix and bastite. The siderophile elements Ni and Cr are enriched in the matrix in comparison to the bastite (Fig. 3, Table SM1). In MVE15-17-3, the FME are all above detection limits, and similar within error in both green and white areas (Fig. 3, Table SM1). Nickel and Cr are enriched in the green areas relative to the white areas (Fig. 3, Table SM1). In MVE15-17-4, the FME are mostly below detection limit, except for B (Fig. 3, Table SM1), and As in the green areas. Nickel and Cr again show a contrasted distribution: Ni and Cr are enriched in the green areas in comparison to the white areas (Fig. 3, Table SM1).

Sample m52 (Sulabest, Iran) display both matrix and bastite microtextures. Lithium and B are enriched in the bastite in comparison to the matrix, while other FME are below detection limits in both microtextures (Fig. 3, Table SM1). Nickel and Cr have contrasted distribution: Ni is enriched in the matrix in comparison with the bastite, and Cr shows the opposite. Sample Su09-17 mesh matrix has low FME, with only B above detection limits. The Ni and Cr contents are unconclusive as there is only one serpentine microtexture (Table SM1).

5.1.2. OCT ophiolites

The trace element geochemistry of the samples from Brazil has already been published for samples QT31 and QT 80 (Hodel et al., 2019). The B contents of serpentine are in the range 120–210 ppm for these two samples (Table SM1), but some serpentinites from the same area have B content up to ~700 ppm. Both microtextures have similar B contents, with no obvious systematic distribution (Fig. 3). Hodel et al. (2019) pointed out contrasting distribution of other FME related to the microtexture of serpentine, with higher Li and Cs contents in the bastite than in the matrix, and higher As and Sb contents in the matrix that in the bastite (see also Table SM1 and Fig. 3).

To summarize, in the samples displaying both mesh matrix and bastite, Li seems to be systematically higher in the bastite than in the matrix (Fig. 3). Boron does not show similar systematics, but the B concentration in matrix and bastite are close to each other for a given sample (Fig. 3). Arsenic, Sb, and Cr are often below detection limits and therefore no systematic can be inferred. In samples with both mesh matrix and bastite, Cr is systematically and significantly enriched in bastite in comparison to the matrix, while Ni is slightly enriched in the matrix in comparison to the bastite (Fig. 3). Only sample MVE15-17-2 has a matrix enriched in both Ni and Cr, which seems to be typical of Potrero Carrillo outcrop, as the other samples from that locality have green zones systematically enriched in both Ni and Cr as well, in comparison to the white zones (Fig. 3).

5.2. Boron isotopes

All the individual in situ values are reported in Supplementary Material (Table SM3).

Serpentine minerals from Concua (Guatemala) have $\delta^{11}B$ straddling 0‰, ranging from -1.0 ± 1.2 to $+0.3 \pm 1.9$‰ in MVE15-9-2 ($n = 5$), and from -0.8 ± 1.2 to $+1.0 \pm 0.7$‰ in MVE15-9-5 ($n = 4$), in both bastite and the matrix. The vein of diopside cutting MVE15-9-5 has $\delta^{11}B$ in the range -3.4 ± 0.9 to -2.1 ± 0.8‰ ($n = 3$) (Fig. 4).

Sample MVE10-10-1 from Gualan (Guatemala) yields similar results: the $\delta^{11}B$ of the matrix range from -3.0 ± 1.2 to $+7.2 \pm 0.8$‰ ($n = 5$) and that of bastite range from -11.6 ± 1.3 to $+2.6 \pm 2.8$‰ ($n = 6$) (Fig. 4). A single analysis performed on the lizardite + calcite vein yields $\delta^{11}B$ of -15.5 ± 0.6‰ (Table SM3).

Samples from Potrero Carrillo (Guatemala) display an unusual texture consisting white and green areas composed of lizardite ± chrysotile. The green areas of MVE15-17-1b have $\delta^{11}B$ ranging from -5.3 ± 1.0 to $+7.6 \pm 1.1$‰ ($n = 6$), while the white areas range from -6.7 ± 0.6 to $+4.8 \pm 1.1$‰ ($n = 5$). Orange areas, made of serpentine mixed with talc, opal, and Fe—Ni spinel, yield $\delta^{11}B$ of $+1.7 \pm 0.7$ to $+3.1 \pm 1.3$‰ ($n = 4$), and the veins range from -0.4 ± 1.6 to $+4.5 \pm 1.1$‰‰ ($n = 2$) (Fig. 4). In sample MVE15-17-2, both the matrix, the bastite, and the vein have similar B isotopic signatures: the matrix yields $\delta^{11}B$ from $+11.1 \pm 1.1$ to $+13.5 \pm 0.7$‰ ($n = 3$), the bastite yields $\delta^{11}B$

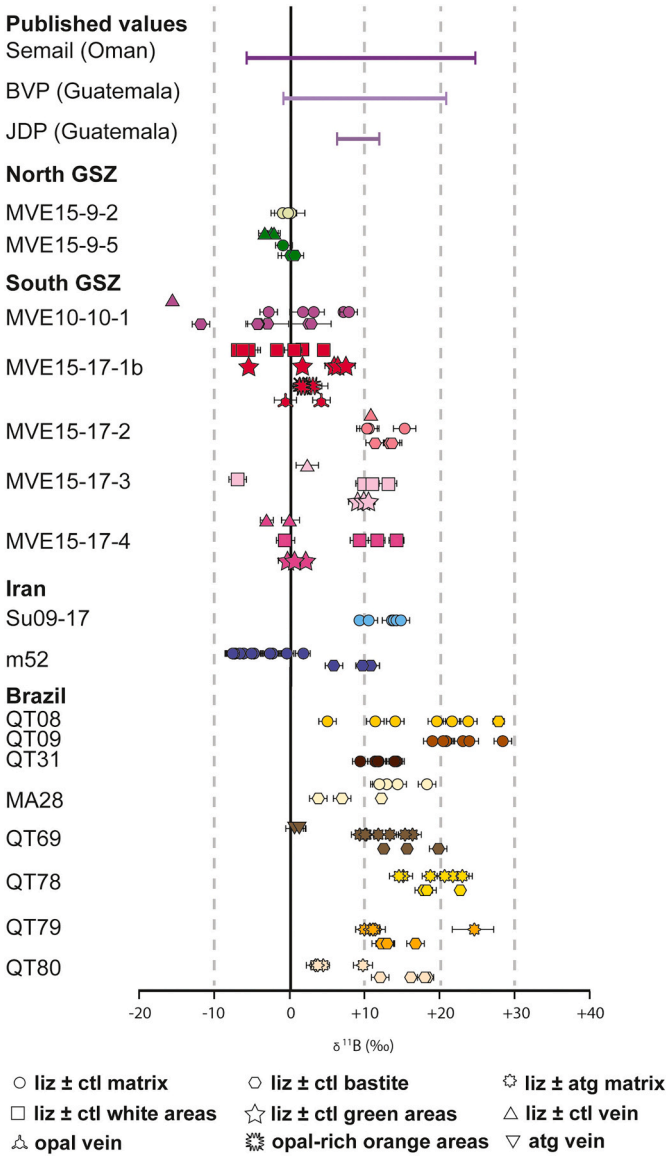

Fig. 4. Individual $\delta^{11}B$ obtained in situ on different minerals/texture of the studied samples. Error bars are always represented, although sometimes they are smaller than the symbol and not visible. The ranges of previously published data on Semail ophiolite, Oman (whole-rocks, Lécuyer et al., 2002 and Prigent et al., 2018), Baja Verapaz and Juan de Paz, Guatemala (in situ, Martin et al., 2016) are also represented.

from +10.1 ± 1.3 to +15.1 ± 1.2‰ ($n = 3$), and the vein single analysis is +10.5 ± 1.3‰ (Fig. 4). In contrast, MVE15-17-3 and MVE1517-4 show slight differences in their B isotopic signature, depending on the location (green or white area) of the analysis (Fig. 4). Sample MVE15-17-3 green areas yield $\delta^{11}B$ from +9.2 ± 1.0 to +10.6 ± 0.9‰ ($n = 3$), the white areas yield $\delta^{11}B$ from −6.7 ± 1.3 to +11.2 ± 1.6‰ ($n = 5$). The one analysis performed in the vein yields $\delta^{11}B$ of +2.4 ± 1.3‰. Similarly, MVE15-17-4 green areas yield $\delta^{11}B$ from +0.1 ± 1.0 to +2.0 ± 1.0‰ ($n = 3$), the white areas yield $\delta^{11}B$ from −0.5 ± 1.3 to +14.5 ± 0.8‰ ($n = 4$), and the vein yields $\delta^{11}B$ ranging from −2.9 ± 1.0 to +0.1 ± 1.3‰ ($n = 2$) (Fig. 4).

Sample Su09-17, from the Sulabest region (Sistan Suture Zone, Iran), yields positive only $\delta^{11}B$, in the range + 9.4 ± 0.8 to +14.1 ± 1.1‰ ($n = 6$). The $\delta^{11}B$ values from sample m52, from the same geological unit, show significant differences depending on the location of the analyses: bastite yields values from +5.8 ± 1.0 to +11.7 ± 1.0‰ ($n = 4$), and matrix yields values from −7.7 ± 1.0 to +1.9 ± 1.1‰ ($n = 13$) (Fig. 4).

Samples from Brazil all have strongly positive $\delta^{11}B$. In the Serra do Quatipuru, QT08 has $\delta^{11}B$ ranging from +5.4 ± 1.1 to +23.9 ± 1.1‰ ($n = 8$) in the matrix, and a single analysis in bastite yields $\delta^{11}B$ of +28.0 ± 1.0‰ (Fig. 4). QT09 matrix has $\delta^{11}B$ ranging from +19.2 ± 1.2 to +28.2 ± 1.3‰ ($n = 6$), and QT31 matrix has $\delta^{11}B$ ranging from +9.8 ± 1.0 to +14.8 ± 1.0‰ ($n = 6$) (Fig. 4). The unique sample from Morro do Agostinho (MA28) studied here shows slight B isotopic differences between the matrix, which yields $\delta^{11}B$ from +12.0 ± 1.0 to +18.2 ± 1.0‰ ($n = 4$), and the bastite which yields $\delta^{11}B$ from +3.7 ± 1.1 to +12.3 ± 1.1‰ ($n = 3$) (Fig. 4). Samples from Serra do Tapa are the only ones to contain some antigorite mixed with lizardite. QT69 matrix yields $\delta^{11}B$ from +9.2 ± 1.0 to +16.3 ± 1.0‰ ($n = 7$), the bastite yields $\delta^{11}B$ from +12.7 ± 1.1 to +19.9 ± 1.1‰ ($n = 3$), and the vein yields $\delta^{11}B$ from +0.4 ± 1.0 to +1.1 ± 1.0‰ ($n = 3$) (Fig. 4). QT78 matrix yields $\delta^{11}B$ from +14.8 ± 1.0 to +23.2 ± 1.0‰ ($n = 6$), and the bastite yields $\delta^{11}B$ from +18.0 ± 1.2 to +23.0 ± 1.1‰ ($n = 3$) (Fig. 4). QT79 matrix yields $\delta^{11}B$ from +10.1 ± 1.0 to +24.8 ± 3.0‰ ($n = 5$), and the bastite yields $\delta^{11}B$ from +12.7 ± 1.0 to +17.1 ± 1.0‰ ($n = 4$) (Fig. 4). QT80 matrix yields $\delta^{11}B$ from +3.8 ± 0.7 to +9.9 ± 1.0‰ ($n = 4$), and the bastite yields $\delta^{11}B$ from +12.3 ± 1.2 to +18.7 ± 1.1‰ ($n = 4$) (Fig. 4).

6. Discussion

6.1. Trace element signatures of the different microtextures of serpentine minerals

Most of the samples studied here (except MVE15-9-2 from Guatemala, and Su09-17 from Iran) display several serpentine minerals microtextures: either mesh matrix and bastite texture, or a patchy texture made of green and white areas, and some are serpentine veins (Table 1). Samples with a mesh matrix and bastite porphyroblasts in which the siderophile elements have been measured (MVE15-9-5, MVE10-10-1, MVE15-17-2, m52) show different features. In MVE15-9-5 and m52, Cr is enriched and Ni is depleted in the bastite in comparison to the mesh matrix (Fig. 3) This probably reflects the composition of the precursor minerals, as suggested by Orberger et al. (1999) and Deschamps et al. (2013). Indeed, orthopyroxene, which is known to be the precursor of bastite (e.g., Mével, 2003), is usually depleted in Ni and enriched in Cr in comparison to olivine (e.g., Stosch, 1981). In contrast, mesh matrix and bastites in MVE10-10-1 have similar Ni and Cr contents, which is similar to features observed in slab serpentinites from the Lanzo Ultramafic massif (Western Alps), where it has been interpreted as representing a homogenization of the inherited composition with increasing serpentinization (Debret et al., 2013), although these rocks are subducted slab serpentinites. Sample MVE15-17-2 has both Cr and Ni enriched in the mesh matrix in comparison to the bastite. Similarly, samples MVE15-17-3 and MVE15-17-4, from the same outcrop, also have the green patches enriched in Cr and Ni in comparison to the white patches (Fig. 3), although these samples do not show the mesh and bastite texture. In contrast, sample MVE15-17-1b, also from the same outcrop, has similar Cr and Ni contents in both green and white patches, but the Cr contents are variable, as shown by the great uncertainties on the averages (Tables SM1 and SM2). The orange areas (Fig. 3), which consist of a mixture of serpentine, talc, and opal, have significantly lower Ni and Cr concentrations than the white and green areas. This MVE15-17 outcrop from the southern GSZ, therefore, has both unusual texture and an intriguing Cr and Ni distribution. Several papers indicate that olivine is preferentially altered below ~400 °C, while orthopyroxene is altered above ~400 °C (e.g., Deschamps et al., 2010; Mével, 2003). In particular, a detailed study conducted on the present-day seafloor — focusing on exhumed altered peridotites from the Southern Wall of the Atlantis Massif — highlighted that at temperatures higher than 350 °C, orthopyroxene is altered prior to olivine, and transformed into tremolite, talc, and/or chlorite. Below 350 °C, olivine and pyroxene transform simultaneously into serpentine polysomes (Rouméjon et al., 2018a). Sample MVE15-17-1b indeed contains chlorite and some talc mixed with lizardite, and no mesh or bastite texture, and some antigorite needles have been identified in MVE15-17-3, suggesting temperatures around 300–350 °C. Thus, the unusual texture of samples from the southern GSZ may reflect alteration starting above 350 °C. This may also explain the Cr and Ni patterns observed in most samples from this outcrop: if the orthopyroxene broke down first, it releases Cr that may be incorporated in the product of olivine breakdowns. The former olivine is therefore enriched in both Cr and Ni (mesh matrix in MVE15-17-2, and green patches in MVE15-7-3 and MVE15-17-4), and the former pyroxene is depleted in these elements.

The FME are expected to represent the signature of the fluid(s) responsible for serpentinization, as the ultramafic protoliths are depleted in these elements, particularly Li and B (e.g., Benton et al., 2004, 2001; Deschamps et al., 2013). All samples studied here exhibit various concentrations of FME. In MVE15-9-5, MVE15-17-2, MVE15-17-3, and QT80, all serpentine microtextures within a given sample have similar FME contents (Fig. 3). This likely indicates a single, massive influx of fluid was responsible for the extensive serpentinization, and consequent homogenization of the FME contents within the rock. This hypothesis is supported by the interpretations that serpentinization / mesh texture develops in two steps: the first one corresponds to low water/rock ratio, and only a couple of veins are visible through the samples, while the second step corresponds to pervasive serpentinization, at high water/rock ratio (e.g., Debret et al., 2013; Viti and Mellini, 1998). In our case, none of the samples with multiple serpentinite microtextures contains any inherited ultramafic silicates, indicating complete or nearly complete serpentinization consistent with the second step mentioned above. In all the other samples, the different microtextures have different concentrations in one or more of the FME (Fig. 3, Table SM1). In samples displaying white and green patches (MVE15-17-1b, and MVE15-17-4), which we attribute to successive alteration of pyroxene then olivine, diachronic alteration can account for the different microtextures having different FME contents (Rouméjon et al., 2018a). Because there is a sequence of hydration steps, the fluid responsible for pyroxene alteration had a different composition than the fluid responsible for olivine alteration. For the three other samples (MVE10-10-1, m52, and QT31), the textures consist of mesh matrix and bastite, which are expected to form simultaneously (Rouméjon et al., 2018a), so the differences in contents observed among the matrix and the bastite are difficult to reconcile. The hypothesis of heterogeneities inherited from precursor minerals is ruled out, as ultramafic olivine and pyroxene have low FME contents, particularly for B that is usually below 1.2 ppm (e.g., Debret et al., 2013; Pabst et al., 2012). In comparison, B in MVE10-10-1, m52, and QT31 varies from 24 to 134 ppm (Table SM1). The fact that the variations observed among the different microtextures are different, i.e., that sometimes B and Li co-vary (m52), and sometimes the opposite (MVE10-10-1 and QT31), likely indicates that these variations are not related to any systematic process, like equilibrium partitioning. Thus, the most likely hypothesis to explain the differences in

FME between mesh and bastite is that these textures did not form simultaneously, on the contrary to the hypothesis suggested by Rouméjon et al. (2018a), and that different fluids were therefore responsible for serpentinization of the different microtextures.

6.2. Boron isotopic signatures of the different microtextures of serpentine

Only a few investigations have studied the variation in isotopic signatures from different microtextures of serpentine within a given sample, and to our knowledge, none have been conducted on B isotopes. In these studies, the authors observed heterogeneities similar to what we show in the present paper. The first, conducted on dredged samples from Southern Indian Ridge, highlights that the δ^{6}Li of distinct serpentine pseudomorphs after pyroxene and olivine are highly heterogeneous and overlapping, which is interpreted as a variation of the isotopic fractionation factor between mineral and fluid coupled with variations of fluid composition (Decitre et al., 2002). The second one, conducted on drilled samples from Atlantis Massif and dredged samples from the Southern Indian Ridge, highlights that the δ^{18}O of mesh cores, mesh rims, and bastite (which all represent primary alteration) all overlap, but with great heterogeneities. Mesh rim O isotopic signatures are completely heterogeneous, mesh core and bastite are moderately heterogeneous, while recrystallized chrysotile, antigorite, and serpentine veins show lower and more homogeneous δ^{18}O. These results are interpreted as a decrease and homogenization of δ^{18}O with increasing time-integrated water/rock ratio at nearly constant temperature (Rouméjon et al., 2018b). Broadly summarized, both studies concluded that the observed heterogeneities in the isotopic signatures of early serpentine microtextures are due to only local equilibrations between fluid (which may evolve in isotopic composition) and serpentine precursor.

The serpentinite samples analyzed here also show differences in the B isotopic data. More than half of the samples (nine out of seventeen: MVE10-10-1, MVE15-17-1b, MVE15-17-3, MVE15-17-4, QT08, QT09, MA28, QT69, and QT78) displays a wide range of δ^{11}B within a single sample, and sometimes even within a given microtexture, and the δ^{11}B of the different microtextures overlap (Table SM3, Fig. 4). Samples QT08, QT09, and QT31 display mesh matrix and bastite, but only the

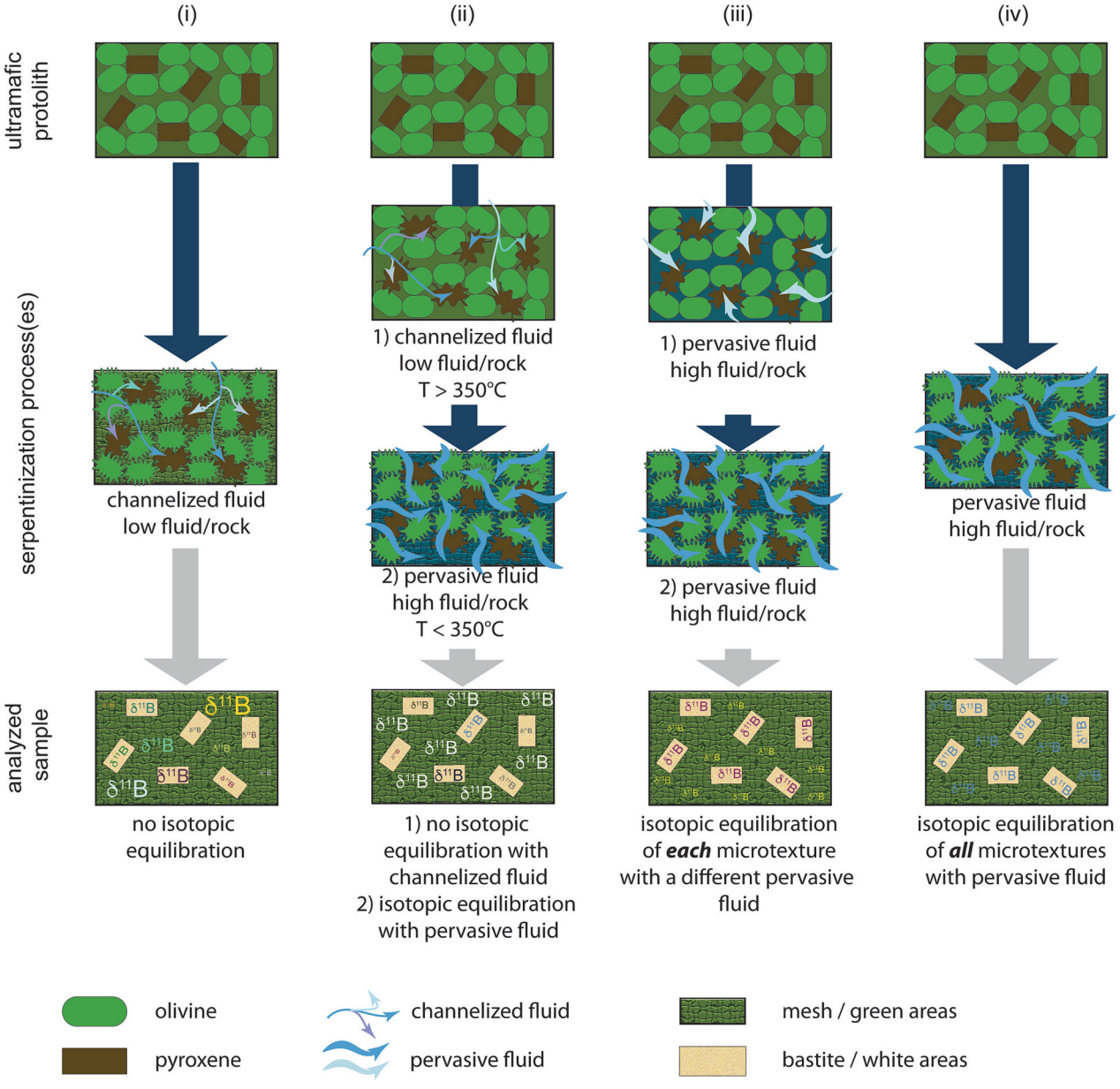

Fig. 5. Cartoon displaying the different possibilities explaining the isotopic compositions observed in ophiolitic serpentinites. See text for details.

matrices have been analyzed for B isotopes. These three samples are therefore not discussed in this paragraph. In the six samples displaying strong isotopic heterogeneities for which both microtextures have been analyzed, all completely serpentinized, two groups can be distinguished. The first group, consisting of samples MVE10-10-1 and QT69 with both matrix and bastite, shows a wide range of $\delta^{11}B$ in both the matrix and bastite. This suggests that none of these samples have undergone a single-stage serpentinization, but rather successive influxes of localized fluids (Fig. 5, i), probably with a different elemental and B isotopic composition (Table SM2) that never equilibrated at the scale of the rock. However, the vein of antigorite cutting QT69 is homogeneous, and isotopically significantly different than the host-rock (Table SM3), indicating a later, more homogeneous fluid. The second group, made of samples MVE15-17-1b, MVE15-17-3, and MVE15-17-4 from the southern GSZ in Guatemala, as well as samples MA28 and QT78 from Brazil, shows one microtexture isotopically homogeneous in B and one or more microtexture(s) with a wide range of B isotopic variations. The homogeneous microtextures are the orange areas in MVE15-17-1b, which may have crystallized directly from the fluid, as indicated by the presence of chrysotile, the green areas in MVE15-17-3 and MVE15-17-4, supposedly after olivine, the matrix in MA28, and the bastite in QT78. For all these microtextures, all the isotopic analyses overlap within errors (Table SM3). The microtexture(s) with heterogeneous isotopic values are the white and green areas in MVE15-17-1b, the white areas in MVE15-17-3 and MVE15-17-4, which we interpret to be after pyroxene, the bastite in MA28, and the matrix in QT78). All these microtextures have a great range of $\delta^{11}B$ signatures, up to 18‰ of variation in MVE15-17-3 (Table SM3). We suggested above that in samples from southern GSZ, white areas formed first, at slightly higher temperature than the green areas. Isotopic results seem in agreement with this interpretation: the first influxes of fluid(s) are localized and do not achieve full isotopic equilibration of the serpentine after pyroxene, but when the fluid/rock ratio increases, the transformation of olivine into serpentine yields homogeneous $\delta^{11}B$ within a given sample (Fig. 5, ii), in agreement with what Rouméjon et al. (2018b) suggested. MVE15-17-1b has a more complex texture, with three microtextures of serpentine minerals. The white areas have a great range of variation (up to 12‰), typical of localized influxes of fluid that do not fully equilibrate with the rock. The green areas have one outlier value ($\delta^{11}B = -5.7$‰, Table SM3), but the other values fall in a narrow range, indicating an increase in the fluid/rock ratio, even if full equilibrium may not have been attained. Finally, the orange areas have homogeneous $\delta^{11}B$, related to an influx of pervasive fluid, which was likely also responsible for opal crystallization. MA28 and QT78 probably also record the transition from low fluid/rock ratio to higher fluid/rock ratio, but it is surprising to notice that the isotopically homogeneous microtexture is different in each sample, particularly as both microtextures are interpreted to form simultaneously (Rouméjon et al., 2018a).

For three samples (m52, QT79, and QT80), the mesh matrix and the bastite isotopic signatures are distinct (Table SM3, Fig. 4). To the best of our knowledge, this has never been reported in literature. The range of $\delta^{11}B$ in a given microtexture is moderate (typically within ~6‰, with an occasional outlier value, as in the bastite of QT80, Table SM3). This is clearly different to what was observed in the samples discussed above, where the values were scattered with wide and overlapping $\delta^{11}B$ variations. The hypothesis that the distinct B isotopic signatures observed in the different microtextures of m52, QT79, and QT80 may be due to the first, localized influx of fluids must, therefore, be ruled out. Three other hypotheses can be considered. First, the bastite and the mesh matrix formed at different times and represent two different fluids (Fig. 5, iii). This may be true in particular for m52, where both the FME and B isotopic signature are distinctly different in the mesh matrix and the bastite (Fig. 4). In addition, this sample is the one for which the gap between mesh matrix B isotopic signature and bastite B isotopic signature is the greatest (~4‰). The second hypothesis is that the samples underwent a slight change of T and pH while being serpentinized by a single pervasive fluid, like described in (Boschi et al., 2008). In this case, mesh matrix and bastite also have to form at slightly different times, and a single fluid, whose isotopic composition would evolve with slight changes in T and/or pH, is required. A third hypothesis is that the B isotopic fractionation between fluid and serpentine is different depending upon the serpentine precursor (olivine versus pyroxene). This hypothesis may be supported by the fact that the FME contents are similar in both microtextures in QT80 (Fig. 3), and, more importantly, because the mesh matrix (after olivine in the three samples) has a lower $\delta^{11}B$ than the bastite (after pyroxene). More work is necessary to validate or reject this hypothesis, but our preferred hypothesis is the first, i.e., different fluids altered olivine and pyroxene at different times.

Finally, samples MVE15-9-5 from northern GSZ and MVE15-17-2 from southern GSZ in Guatemala, show homogeneous overlapping $\delta^{11}B$ values in both mesh matrix and bastite (Fig. 4, Table SM3). This is consistent with an influx of a single pervasive fluid (Debret et al., 2013), i.e., a high fluid/rock ratio allowing the homogenization of the isotopic signature of the rock (Rouméjon et al., 2018b). Sample MVE15-9-5 indeed shows some recrystallized lizardite (Fig. SM2a, b), indicating an increase in the fluid/rock ratio (Rouméjon et al., 2018a). Interestingly, MVE15-9-2, collected in close vicinity of MVE15-9-5, shows only a homogeneous matrix (Table SM2), and also has a homogeneous $\delta^{11}B$ signature, with values similar to MVE15-9-5. This is another argument in favor of a single pervasive fluid widely distributed at the outcrop scale (Fig. 5, iv).

To summarize, the distribution of $\delta^{11}B$ among the different microtextures of serpentine is not well constrained and more work is necessary to fully understand the processes that occurred during serpentinization of the mantle and the associated B isotopic fractionation. However, this study highlights four possible scenarios (Fig. 5):

(i) All serpentine microtextures have wide ranges of $\delta^{11}B$ that overlap, which likely indicates that serpentinization occurred at low fluid/rock ratios by channelized fluids. The wide ranges of $\delta^{11}B$ observed may be due to a lack of isotopic equilibration, successive fluids with different B isotopic signatures, or both.

(ii) Different serpentine microtextures have overlapping $\delta^{11}B$, but one microtexture has a significantly narrower range than the other(s). This has been primarily observed in the samples from the southern GSZ in Guatemala, which are inferred to have been serpentinized in two steps, following interpretations of Rouméjon et al. (2018a): first, the pyroxene breaks down (above 350 °C) to serpentine + chlorite, then the olivine breaks down (below 350 °C) to serpentine. The B isotopic signatures are consistent with this hypothesis. Serpentine + chlorite mixtures after pyroxene display the highly variable $\delta^{11}B$, with an interpretation similar to (i), whereas the serpentine after olivine has a narrower range of $\delta^{11}B$, which is interpreted as homogenization at high fluid/rock ratios (Rouméjon et al., 2018b). Interestingly, samples with the more common mesh and bastite texture show similar isotopic features (one microtexture heterogenous, and one homogeneous), suggesting that the formation of mesh and bastite is not systematically synchronous.

(iii) The different microtextures of serpentine in a given sample have moderately variable $\delta^{11}B$ that do not overlap. This has never been reported in literature, and the best hypothesis is that successive pervasive fluids are responsible for serpentinization of the different microtextures. The sequence may be coupled with variation of temperatures, as suggested by Rouméjon et al. (2018a), even if the classical mesh and bastite textures are observed. Otherwise, some unknown process or processes are required.

(iv) All serpentine microtextures have narrow ranges of $\delta^{11}B$ that overlap, which is interpreted as the product of a single pervasive fluid (i.e., high fluid/rock ratio; Rouméjon et al., 2018b) yielding an isotopically homogeneous serpentinization of the rock.

6.3. Sources of the fluid(s) responsible for serpentinization of the ophiolitic mantle

The B isotopic signature of serpentine minerals in obducted ophiolites is quite variable, as shown above. Hence, with the exception of samples MVE10-10-1, QT08, QT09, and QT69, which display wide variations in $\delta^{11}B$ and may be out of equilibrium, the other samples, or at least one serpentine microtexture of the sample, can be used to track down the source(s) of the fluid responsible for serpentinization. Previously published samples from Baja Verapaz (BVP) and Juan de Paz (JdP), Guatemala, have homogeneous B isotopic signatures (Martin et al., 2016) and are also considered in the following discussion on the tracking of the source(s) of fluid responsible for serpentinization of ophiolite. All these samples either have homogeneous or moderately variable $\delta^{11}B$, generally within a range of 6‰ for a given sample or a given microtexture within a sample, which is typically what was previously observed in samples for which it was possible to determine the source(s) of the fluid (see Martin et al., 2016, 2020). Recently, Martin et al. (2020) suggested that serpentine minerals or serpentinites with $\delta^{11}B$ above +10‰ have been serpentinized by seawater-derived fluid, while serpentine minerals or serpentinites with $\delta^{11}B$ below +10‰ have been serpentinized by subducted crust-related metamorphic fluid.

6.3.1. Serpentinites from SSZ ophiolites

In samples from Guatemala and Iran, the $\delta^{11}B$ of serpentinites ranges from −7.7 to +15.1‰‰ (Table SM3), which is in agreement with previously published values in serpentinites from SSZ ophiolites, which range from −5.7 to +25.1‰ (Fig. 4, Fig. 6a; Lécuyer et al., 2002, Martin et al., 2016, Prigent et al., 2018). The B isotopic results presented here for SSZ obducted ophiolites, as well as previously published values on ophiolitic serpentinites from the Semail Ophiolite (Oman) and the Baja Verapaz and Juan de Paz Ophiolites (Guatemala), are distributed on both sides of the $\delta^{11}B = +10$‰ threshold (Fig. 6a, b, c, d), indicating that both types of fluid have been involved in the ophiolite serpentinization process. Are these fluids mixed prior to serpentinization, or are there successive influxes of fluid from both sources?

On a histogram of frequencies, serpentinites forming from either seawater or subducted crust-related metamorphic fluids show a bimodal distribution, with the maximum frequency for serpentinites forming from seawater for $\delta^{11}B$ in the range +10 to +20‰, while serpentinites forming from subducted crust-related metamorphic fluids peak at $\delta^{11}B$ of 0 to −10‰ (Fig. 7a). Interestingly, the $\delta^{11}B$ peak observed for ophiolitic serpentinites is in the range −5 to +15‰, partly where the relative frequency of seawater- or subducted crust-related metamorphic fluid serpentinites is the lowest (Fig. 7a). This suggests that, in samples/textures with homogeneous B isotopic signatures, both fluids have been mixed, in different proportions, prior to serpentinization. If serpentinization had occurred from successive influxes, either the last influx would erase previous signature, or the signature would likely be heterogeneous, as suggested above and on Fig. 5. Only m52 may testify of two successive fluids at equilibrium (see below). A tentative model, using the equations of B isotopes partitioning between aqueous fluid and phyllosilicate (Wunder et al., 2005), has been implemented to estimate the $\delta^{11}B$ signatures of serpentinites formed from endmembers fluids (either seawater or subducted crust-related metamorphic fluid with $\delta^{11}B$ of −5‰, see Supplementary Material 4 for the discussion about the $\delta^{11}B$ value for the subducted crust-related metamorphic fluid) and from a mixing of both fluids in different ratios (see details on the equations and parameters used for the modeling in Supplementary Material 4). However, a subducted crust-related metamorphic fluid with a $\delta^{11}B$ of −5‰ represents only one possible scenario. Any significant change in the $\delta^{11}B$ of the initial metamorphic rock, the pH, the temperature, or the mineralogy of the initial metamorphic rock may have dramatic effect on the $\delta^{11}B$ released by the metamorphic rock, and the $\delta^{11}B$ of the mixture with seawater. An example of mixing between the same fluids with a basic pH is presented in Supplementary Material 4, Fig. SM4-1.

The samples with a homogeneous $\delta^{11}B$ signature independent of the microtexture, or the samples without visible microtextures likely only experienced a single influx of pervasive fluid, as discussed above. Samples MVE15-9-2 and MVE15-9-5, as well as a sample (matrix) from BVP (MVE12-39-1 — see Martin et al., 2016) have $\delta^{11}B$ straddling 0‰ (Fig. 6a, b), and the model suggests – with the considered parameters – that the fluid would most likely be a mixture of seawater with 30 to 60% of subducted crust-related metamorphic fluid with $\delta^{11}B$ of −5‰ (Fig. 7b). Alternatively, it is possible that shallow subducted crust-related metamorphic fluids have less fractionated B isotopic signatures (e.g., Bebout and Nakamura, 2003; Yamada et al., 2019b) and that the $\delta^{11}B$ of the serpentine minerals forming from these fluids will be less negative than the one forming at greater depths or slightly positive, in the range of what is observed for these three samples. Similarly, sample MVE15-17-2 has $\delta^{11}B$ between +10 and +15‰ (Fig. 6c), in the field of serpentine forming from seawater-derived fluid. The model also show that these values may correspond to serpentinites that have been altered by a mixture of seawater and 30–40% of subducted crust-related metamorphic fluid (Fig. 4e). Previously published sample MVE12-30-4 (Martin et al., 2016), from BVP (Guatemala) has $\delta^{11}B$ between +4 and +6‰ (Fig. 6a), suggesting that this serpentinite has been altered with seawater mixed with 10–40% of subducted crust-related metamorphic fluid (Fig. 7b). Finally, sample Su09-17 from Sulabest (Iran) and a previously published sample from JdP (MVE10-16-3, Guatemala, Martin et al., 2016) has $\delta^{11}B$ straddling +10‰ (Fig. 6a, d), suggesting the fluid responsible for serpentinization was predominantly seawater, with possibly a maximum of ~30% of subducted crust-related metamorphic fluid with $\delta^{11}B$ of −5‰, according to the modeling (Fig. 7b).

The other samples have distinct isotopic signatures depending on the microtexture. Among them, samples m52 is interpreted as having recorded different fluids in its different microtextures: m52 mesh texture may have formed from a mixture of fluids containing between 20 and 70% of subducted crust-related metamorphic fluid with $\delta^{11}B$ of −5‰ (Fig. 7c), or from shallow subducted crust-related metamorphic fluid, as described above. The bastite texture formed from a fluid that could be nearly seawater-derived fluid only or a mixture of seawater with up to ~40% of subducted crust-related metamorphic fluid, depending on the temperature (Fig. 7c). Finally, samples MVE15-17-1b, MVE15-17-3, and MVE15-17-4 have only one microtexture with $\delta^{11}B$ in equilibrium. It is impossible to determine if the difference between the microtextures is due to different influxes of fluid, or to an increase of the fluid/rock ratio during serpentinization. Whatever the scenario considered, the isotopically homogeneous phase in samples from south GSZ, Guatemala testifies to a strong influence of subducted crust-related metamorphic fluid mixed with seawater (~ 50–60% of metamorphic fluids in MVE15-17-1b and MVE15-17-4, and ~30–50% in MVE15-17-3, Fig. 7c). The hypothesis of a shallow subducted crust-related metamorphic fluid can also be considered for samples MVE15-17-1b and MVE15-17-4.

Thus, it seems that for most SSZ ophiolite serpentinite samples, the mixing of both fluids in variable proportions occurred prior to serpentinization, with the possible exception of samples MVE15-17-2 and the bastite microtexture in m52, which could have formed from seawater-derived fluid only. For the samples whose B isotopic signature straddles 0‰, the hypothesis of shallow subducted crust-related metamorphic fluids, yielding slightly positive to slightly negative serpentinites, may also be considered, although the actual value of $\delta^{11}B$ in serpentinite cannot be directly linked to the depth of serpentinization (see Supplementary Material SM4 for details). Additionally, serpentinites with $\delta^{11}B$ in the range 0 to + 5‰ are the least common among serpentinites forming from subducted crust-related metamorphic fluids, while these values are overrepresented for ophiolites (Fig. 7a).

6.3.2. Samples from OCT ophiolites

Samples from Brazil represent obducted ophiolite forming in passive margins, in an ocean-continent transition. Their $\delta^{11}B$ ranges from +3.8 to +24.8‰ (Fig. 6e; Table SM3), also within the range of $\delta^{11}B$ measured

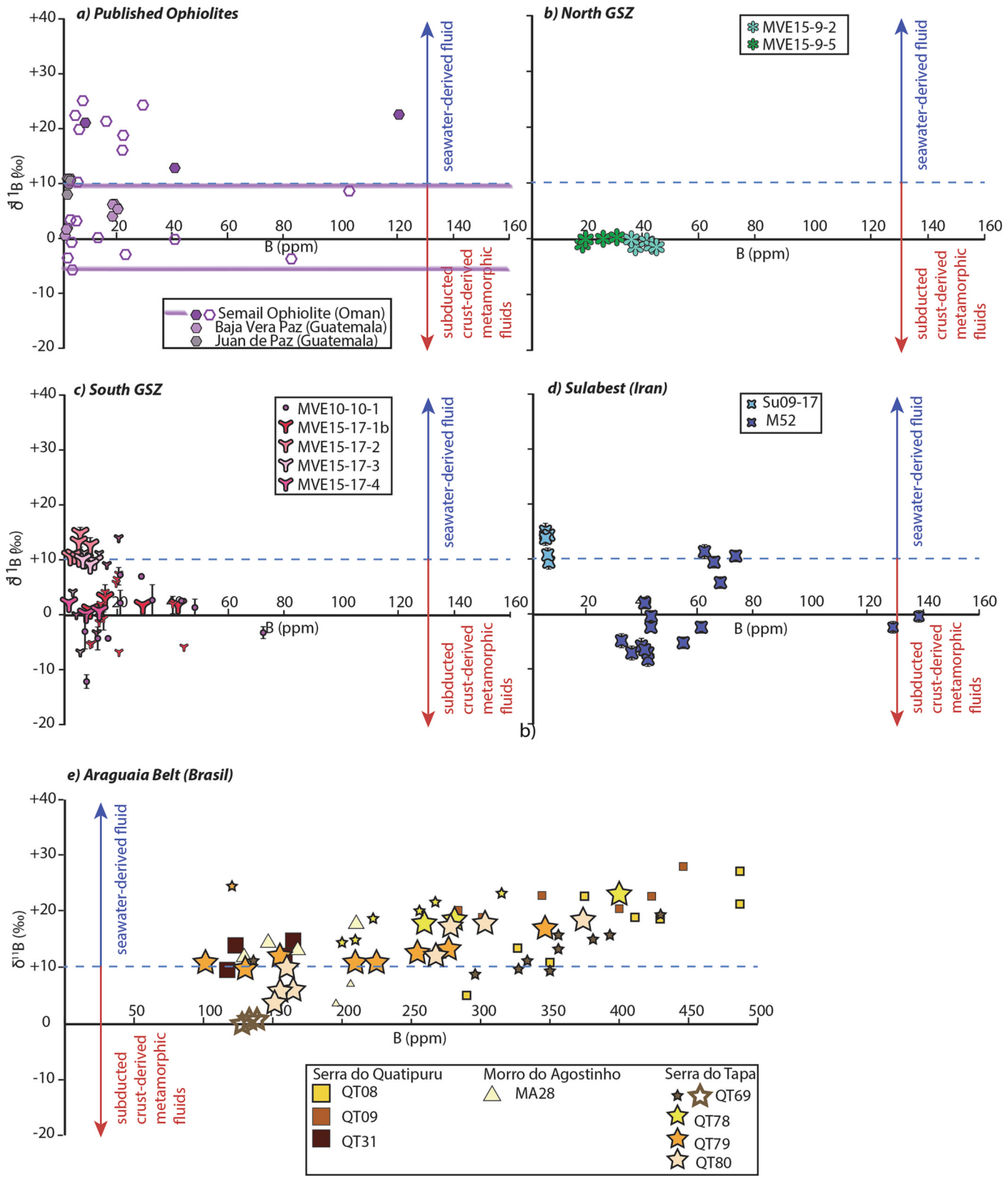

Fig. 6. $\delta^{11}B$ vs. B contents diagrams for the serpentinite samples from ophiolite a) published ophiolites (whole-rock Oman data from Lécuyer et al. (2002), for which only the minimum and maximum values are represented by lines, as no B content was available, and from Prigent et al. (2018), with full symbols representing fully serpentinized samples, and open symbols representing partly serpentinized ones; in situ Baja Verapaz and Juan de Paz matrix values from Martin et al. (2016)), b) data from northern GSZ, c) data from southern GSZ, d) data from Sulabest area (Sistan, Eastern Iran), and e) data from Brazil. Small symbols are for data that are too heterogeneous to be considered in the identification of the fluid source, open symbols are for veins.

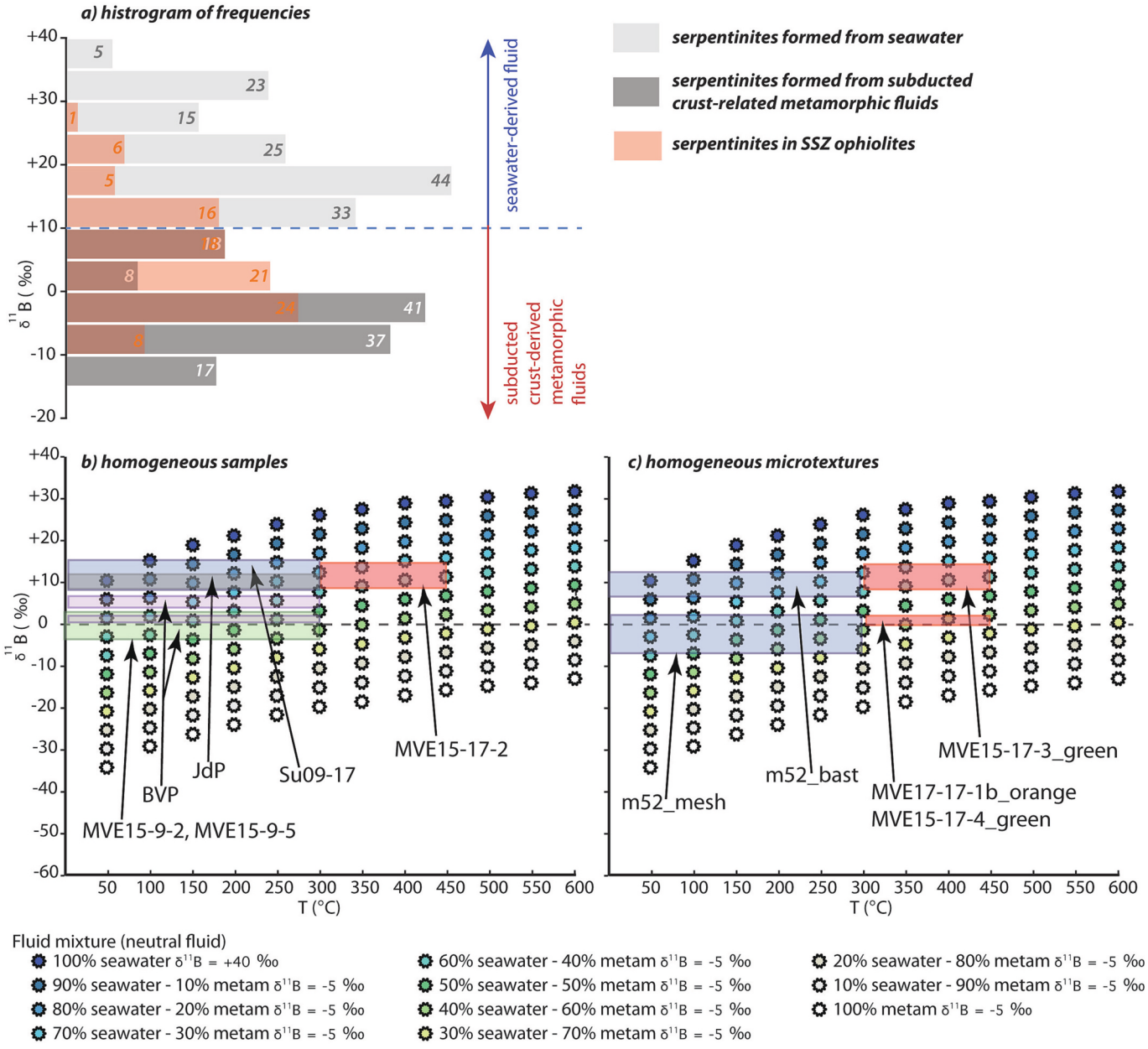

Fig. 7. a) A distribution of δ11B values from serpentinites formed from known fluids (seawater and subducted crust-derived metamorphic fluids) and of serpentinites found in SSZ ophiolites. Data for serpentinites formed from seawater are from Boschi et al. (2013, 2008); Cannaò et al. (2016); Harvey et al. (2014a, 2014b); Martin et al. (2020); Scambelluri and Tonarini (2012); Spivack and Edmond (1987); Vils et al. (2009), data for serpentinites formed from subducted crust-derived metamorphic fluids are from Cannaò et al. (2015); Martin et al. (2020); Peacock and Hervig (1999), data for serpentinite in ophiolites are from Lécuyer et al. (2002); Martin et al. (2016); Prigent et al. (2018), and the present paper. The $\delta^{11}B = +10‰$ threshold is taken from Martin et al. (2020), the numbers written on each bar of the histogram represent the *n* number of data for a given range. Fig. 7b–c: $\delta^{11}B$ of serpentinites forming from fluids varying from 100% seawater to 100% subducted crust-derived metamorphic neutral fluid at temperature from 50 to 600 °C and comparison with measured values, modeled using the B isotopes partitioning between aqueous fluid and phyllosilicates equations of Wunder et al. (2005). b) samples showing a single, homogeneous B isotopic signature and previously published samples from Guatemala, c) samples showing two distinct B isotopic signatures or only one homogeneous microtexture.

in serpentinites from ophiolites ($\delta^{11}B$ from −5.7 to +25.1‰; Fig. 6a; Lécuyer et al., 2002, Martin et al., 2016, Prigent et al., 2018). However, these samples lack negative values, and with the exception of matrix data in QT80, all $\delta^{11}B$ are above +10‰ (Fig. 6e). Such results (no negative values, and barely any below the +10‰ threshold) are even in better agreement with serpentinites hydrated by seawater and seawater-derived fluids, as seen in Martin et al. (2020) and on the histogram (Fig. 7a), even if the B content of Brazilian serpentinites are among the highest measured, and the reason for that is still unknown. Thus, OCT serpentinites have been hydrated by seawater or seawater-derived only, as expected for passive margins.

These observations partly contradict the interpretation of all papers previously published, as the authors alternately suggested that seawater alone was responsible for serpentinization of the peridotite found in obducted ophiolites (Agranier et al., 2007; Lécuyer et al., 2002; Li and Lee, 2006; Martin et al., 2016) or subducted crust-related metamorphic fluid only (Prigent et al., 2018). If serpentinites in OCT ophiolites are indeed hydrated by seawater only, serpentinites in SSZ ophiolites are hydrated by a mixture of seawater and subducted crust-related metamorphic fluids in various proportions, and the mixing of fluids apparently occurred prior serpentinization in most cases.

6.4. Tectonic settings of SSZ ophiolites

As discussed above, the B isotopic signature of serpentine minerals in SSZ ophiolites is mostly distinct from serpentinites from other origins, and likely results from the influence of both seawater-derived fluids and subducted crust-related metamorphic fluids, possibly mixed prior to serpentinization.

The locations in which seawater or seawater-derived fluids and subducted crust-related metamorphic fluids can be mixed prior entering ultramafic rocks are represented on Fig. 8. First, subduction initiation (Fig. 8a) would allow the mixing of seawater, percolating through the oceanic crust, and early subducted crust-related metamorphic fluids released from the downgoing slab. Such a setting has previously been considered to explain formation of Oman SSZ ophiolite and the associated slightly negative to moderately positive B isotopic signatures (Prigent et al., 2018). Alternatively, assuming that shallow subducted crust-related metamorphic fluids indeed have a less negative to slightly positive $\delta^{11}B$ (because they are less fractionated than deeper, strictly negative fluids), this setting would also explain the B isotopic signatures observed for serpentinites in SSZ ophiolites, even without seawater percolation. Similarly, an early forearc setting (Fig. 8b) would facilitate the mixing – in variable proportions – of seawater percolating through the oceanic crust and of subducted crust-related metamorphic fluids released from the downgoing slab. This assessment is consistent with the papers suggesting that SSZ ophiolites represent ancient forearc lithosphere (Stern et al., 2012). Finally, fully developed back-arcs with spreading center (Fig. 8c), which have been suggested to be the setting in which SSZ ophiolites form (Dewey, 1976; Pearce, 2003), are also good candidates to explain fluids mixing prior serpentinization. The relative proximity of the spreading center, which is the most likely location for seawater percolation (see Fig. 8a insert), and of slab subduction, would facilitate the mixing of both seawater-derived and subducting crust-derived fluids, yielding the observed $\delta^{11}B$ in SSZ serpentinites.

7. Conclusions

- The $\delta^{11}B$ of serpentine minerals found in altered ultramafic rocks in SSZ ophiolitic complexes from Guatemala and Iran varies from –7.5 to +15‰. This range of values straddles the $\delta^{11}B = +10‰$ threshold previously argued as the boundary between seawater-derived fluids (above +10‰) and subducted crust-related metamorphic fluid (below +10‰), suggesting that the fluids responsible for serpentinization in SSZ ophiolite are both seawater-derived and metamorphism-derived from subducted oceanic crust.
- The B isotopic signatures of most of the SSZ samples studied here indicate that the fluids from both sources have been possibly mixed prior serpentinization. Such a mixing is inconsistent with a mid-

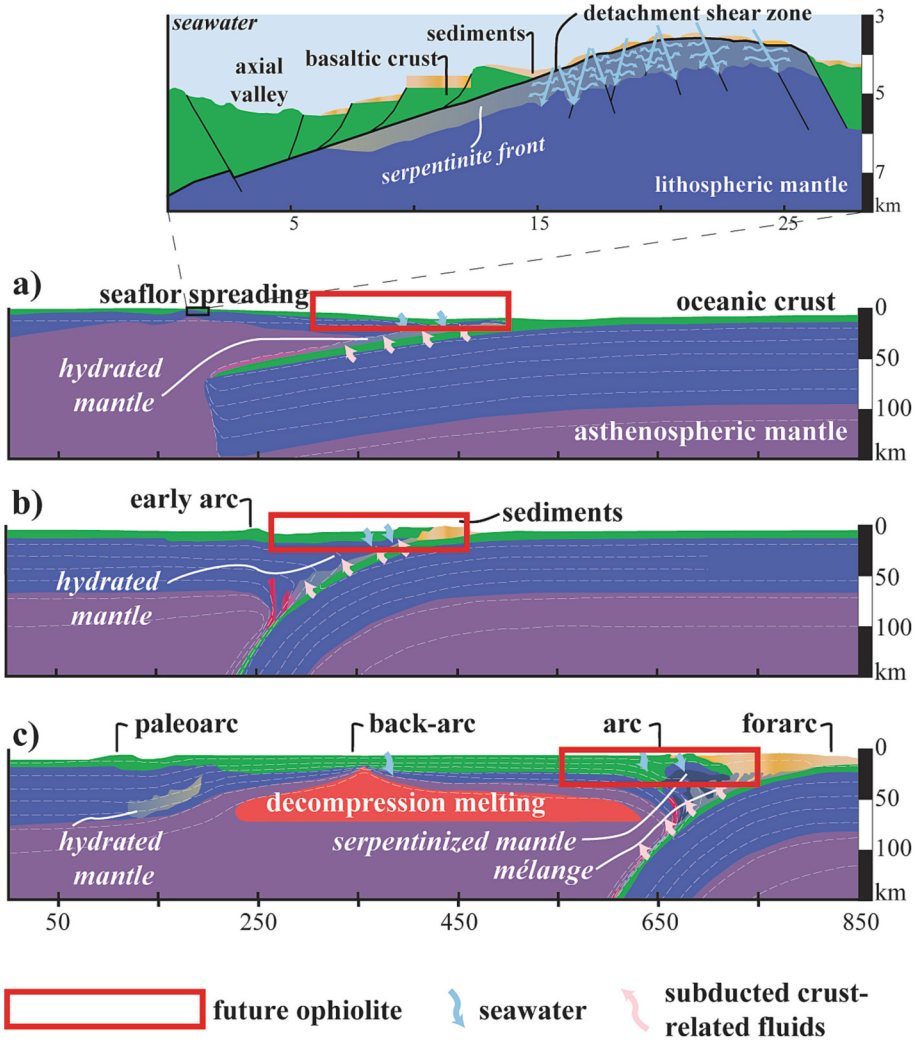

Fig. 8. Schematic representation of the different settings in which future ophiolite can form and be hydrated: (a) subduction initiation with a zoom on serpentinization mechanism at seafloor spreading (b) early arc stage, (c) full arc-back arc system with spreading (Supra Subduction ophiolites). After Baitsch-Ghirardello et al. (2014).

ocean ridge setting, but is instead interpreted as related to subduction initiation, forearc, or back-arc setting.

- The $\delta^{11}B$ of serpentine minerals found in altered ultramafic rocks in OCT ophiolitic complexes from Brazil ranges from +4 to +25‰, similar to the $\delta^{11}B$ of abyssal serpentinites altered by seawater. This confirms that ophiolites representing oceanic lithosphere formed away from subduction zones (at passive margin) have strictly seawater-derived only B isotopic signatures.
- The term ophiolite is often used to designate any sliver of oceanic crust preserved on the continents, regardless of its original setting. This study highlights the fact that the B isotopic signature of SSZ ophiolite serpentinites shows the influence of both seawater and subduction crust-related metamorphic fluid(s), while OCT ophiolite serpentinites only show seawater influence, which could help discriminating the origin of the ophiolite in complicated or reworked settings.
- In most samples, coexisting bastite and mesh textures have different B isotopic signatures. This textural control of B isotope signature has not been previously reported in serpentinites, and raises several questions, in particular about the relative timing of alteration reactions of olivine (to mesh texture) and orthopyroxene (to bastite texture). More work is needed to understand the complex links between fluid/rock ratio, mineral transformation, and isotopic equilibration in ultramafic material.

Supplementary data to this article can be found online at https://doi.org/10.1016/j.lithos.2023.107275.

Declaration of Competing Interest

The authors declare the following financial interests/personal relationships which may be considered as potential competing interests:

Celine Martin reports financial support was provided by National Science Foundation. Kennet Flores reports financial support was provided by National Science Foundation.

Acknowledgments

Reviews from Enrico Cannaò and an anonymous reviewer, as well as edition by Nadia Malaspina significantly helped to improve this manuscript. The authors thank the helpful assistance of Louise Bolge at LDEO facilities and access to the MC-ICPMS by Steve Goldstein, and of Jacob Setera and Linda Godfrey at Rutgers University with the facilities and access to the Laser microscope by Jill van Tongeren. Funding for this project by the US National Science Foundation NSF EAR 1951166 to C. M, EAR 1951172 to K.E.F., and in part by the start-up budget of C.M. at the University of North Carolina at Charlotte is acknowledged. F.H. acknowledge IODP France for his postdoctoral fellowship.

References

Agranier, A., Lee, C.-T.A., Li, Z.-X.A., Leeman, W.P., 2007. Fluid-mobile element budgets in serpentinized oceanic lithospheric mantle: Insights from B, As, Li, Pb, PGEs and Os isotopes in the Feather River Ophiolite, California. Chem. Geol. 245, 230–241. https://doi.org/10.1016/j.chemgeo.2007.08.008.

Alvarenga, C.J.S., Moura, C.A.V., Gorayeb, P.S.S., Abreu, F.A.M., 2000. Paraguay and Araguaia Belts, Tectonic Evolution Of South America. Rio de Janeiro.

Angiboust, S., Agard, P., De Hoog, J.C.M., Omrani, J., Plunder, A., 2013. Insights on deep, accretionary subduction processes from the Sistan ophiolitic "mélange" (Eastern Iran). Lithos 156–159, 139–158. https://doi.org/10.1016/j.lithos.2012.11.007.

Angiboust, S., Pettke, T., De Hoog, J.C., Caron, B., Oncken, O., 2014. Channelized fluid flow and eclogite-facies metasomatism along the subduction shear zone. J. Petrol. 55, 883–916.

Babazadeh, S.A., De Wever, P., 2004. Radiolarian Cretaceous age of Soulabest radiolarites in ophiolite suite of eastern Iran. Bull. Soc. Géol. France 175, 121–129. https://doi.org/10.2113/175.2.121.

Baitsch-Ghirardello, B., Gerya, T.V., Burg, J.-P., 2014. Geodynamic regimes of intra-oceanic subduction: Implications for arc extension vs. shortening processes. Gondwana Res. 25, 546–560. https://doi.org/10.1016/j.gr.2012.11.003.

Barnicoat, A.C., Cartwright, I., 1995. Focused fluid flow during subduction: oxygen isotope data from high-pressure ophiolites of the western Alps. Earth Planet. Sci. Lett. 132, 53–61. https://doi.org/10.1016/0012-821X(95)00040-J.

Bebout, G.E., Nakamura, E., 2003. Record in metamorphic tourmalines of subduction-zone devolatilization and boron cycling. Geology 31, 407–410. https://doi.org/10.1130/0091-7613(2003)031<0407:rimtos>2.0.co;2.

Benton, L.D., Ryan, J.G., Tera, F., 2001. Boron isotope systematics of slab fluids as inferred from a serpentine seamount. Mariana Forearc Earth Planet. Sci. Lett. 187, 273–282.

Benton, L.D., Ryan, J.G., Savov, I.P., 2004. Lithium abundance and isotope systematics of forearc serpentinites, Conical Seamount, Mariana forearc: insights into the mechanics of slab-mantle exchange during subduction: lithium abundance and isotope systematics. Geochem. Geophys. Geosyst. 5 https://doi.org/10.1029/2004GC000708.

Bonnet, G., Agard, P., Angiboust, S., Monié, P., Jentzer, M., Omrani, J., Whitechurch, H., Fournier, M., 2018. Tectonic slicing and mixing processes along the subduction interface: The Sistan example (Eastern Iran). Lithos 310–311, 269–287. https://doi.org/10.1016/j.lithos.2018.04.016.

Boschi, C., Dini, A., Früh-Green, G.L., Kelley, D.S., 2008. Isotopic and element exchange during serpentinization and metasomatism at the Atlantis Massif (MAR 30°N): Insights from B and Sr isotope data. Geochim. Cosmochim. Acta 72, 1801–1823. https://doi.org/10.1016/j.gca.2008.01.013.

Boschi, C., et al., 2013. Serpentinization of mantle peridotites along an uplifted lithospheric section, Mid Atlantic Ridge at 11° N. Lithos 178, 3–23. https://doi.org/10.1016/j.lithos.2013.06.003.

Brueckner, H.K., Lallemant, H.G.A., Sisson, V.B., Harlow, G.E., Hemming, S.R., Martens, U., Tsujimori, T., Sorensen, S.S., 2009. Metamorphic reworking of a high pressure–low temperature mélange along the Motagua fault, Guatemala: a record of Neocomian and Maastrichtian transpressional tectonics. Earth Planet. Sci. Lett. 284, 228–235.

Cannaò, E., Agostini, S., Scambelluri, M., Tonarini, S., Godard, M., 2015. B, Sr and Pb isotope geochemistry of high-pressure Alpine metaperidotites monitors fluid-mediated element recycling during serpentinite dehydration in subduction mélange (Cima di Gagnone, Swiss Central Alps). Geochim. Cosmochim. Acta 163, 80–100. https://doi.org/10.1016/j.gca.2015.04.024.

Cannaò, E., Scambelluri, M., Agostini, S., Tonarini, S., Godard, M., 2016. Linking serpentinite geochemistry with tectonic evolution at the subduction plate-interface: the Voltri Massif case study (Ligurian Western Alps, Italy). Geochim. Cosmochim. Acta 190, 115–133.

Casey, J.F., Dewey, J.F., 1984. Initiation of subduction zones along transform and accreting plate boundaries, triple-junction evolution, and forearc spreading centres-implications for ophiolitic geology and obduction. Geol. Soc. Spec. Publ. 13, 269–290. https://doi.org/10.1144/GSL.SP.1984.013.01.22.

Catanzaro, E.J., 1970. Boric Acid: Isotopic and Assay Standard Reference Materials. National Bureau of Standards, Institute for Materials Research, p. 17.

Daly, M.C., Andrade, V., Barousse, C.A., Costa, R., McDowell, K., Piggott, N., Poole, A.J., 2014. Brasiliano crustal structure and the tectonic setting of the Parnaíba basin of NE Brazil: results of a deep seismic reflection profile. Tectonics 33, 2102–2120. https://doi.org/10.1002/2014TC003632.

Debret, B., Andreani, M., Godard, M., Nicollet, C., Schwartz, S., Lafay, R., 2013. Trace element behavior during serpentinization/de-serpentinization of an eclogitized oceanic lithosphere: a LA-ICPMS study of the Lanzo ultramafic massif (Western Alps). Chem. Geol. 357, 117–133.

Decitre, S., Deloule, E., Reisberg, L., James, R., Agrinier, P., Mével, C., 2002. Behavior of Li and its isotopes during serpentinization of oceanic peridotites. Geochem. Geophys. Geosyst. 3, 1–20. https://doi.org/10.1029/2001GC000178.

Delaloye, M., Desmons, J., 1980. Ophiolites and melange terranes in Iran: a geochronological study and its paleotectonic implications. Tectonophysics 68, 83–111. https://doi.org/10.1016/0040-1951(80)90009-8.

Deschamps, F., Guillot, S., Godard, M., Chauvel, C., Andreani, M., Hattori, K., 2010. In situ characterization of serpentinites from forearc mantle wedges: timing of serpentinization and behavior of fluid-mobile elements in subduction zones. Chem. Geol. 269, 262–277.

Deschamps, F., Godard, M., Guillot, S., Hattori, K., 2013. Geochemistry of subduction zone serpentinites: a review. Lithos 178, 96–127.

Dewey, J.F., 1976. Ophiolite obduction. Tectonophysics 31, 93–120. https://doi.org/10.1016/0040-1951(76)90169-4.

Ernst, W.G., Dal Piaz, G.V., 1978. Mineral parageneses of eclogitic rocks and related mafic schists of the Piemonte ophiolite nappe, Breuil-St. Jacques area, Italian Western Alps. Am. Miner. 63, 621–640.

Flores, K.E., Martens, U.C., Harlow, G.E., Brueckner, H.K., Pearson, N.J., 2013. Jadeitite formed during subduction: *in situ* zircon geochronology constraints from two different tectonic events within the Guatemala Suture Zone. Earth Planet. Sci. Lett. 371, 67–81. https://doi.org/10.1016/j.epsl.2013.04.015.

Flores, K.E., Skora, S., Martin, C., Harlow, G.E., Rodríguez, D., Baumgartner, P.O., 2015. Metamorphic history of riebeckite- and aegirine-augite-bearing high-pressure–low-temperature blocks within the Siuna Serpentinite Mélange, northeastern Nicaragua. Int. Geol. Rev. 57, 943–977. https://doi.org/10.1080/00206814.2015.1027747.

Fotoohi Rad, G.R., Droop, G.T.R., Amini, S., Moazzen, M., 2005. Eclogites and blueschists of the Sistan Suture Zone, eastern Iran: a comparison of P–T histories from a subduction mélange. Lithos 84, 1–24. https://doi.org/10.1016/j.lithos.2005.01.007.

Gangjian, W., Jingxian, W., Ying, L., Ting, K., Zhongyuan, R., Jinlong, M., Yigang, X., 2013. Measurement on high-precision boron isotope of silicate materials by a single column purification method and MC-ICP-MS. J. Anal. At. Spectrom. 28, 606–612.

Gorayeb, P.S.S., 1989. Corpos serpentiníticos da Faixa Araguaia na região de Araguacema- Pequizeiro-Conceição do Araguaia (Goiás-Pará). Rev. Bras. Geociências 19, 51–62.
Gregory, R.T., 2003. Ophiolites and global geochemical cycles: implications for the isotopic evolution of seawater. Geological Society, London, Special Publications 218, 353–368. https://doi.org/10.1144/GSL.SP.2003.218.01.18.
Harlow, G.E., Hemming, S.R., Lallemant, H.G.A., Sisson, V.B., Sorensen, S.S., 2004. Two high-pressure-low-temperature serpentinite-matrix melange belts, Motagua fault zone, Guatemala: a record of Aptian and Maastrichtian collisions. Geology 32, 17–20. https://doi.org/10.1130/g19990.1.
Harvey, J., Garrido, C.J., Savov, I., Agostini, S., Padrón-Navarta, J.A., Marchesi, C., Sánchez-Vizcaíno, V.L., Gómez-Pugnaire, M.T., 2014a. 11 B-rich fluids in subduction zones: the role of antigorite dehydration in subducting slabs and boron isotope heterogeneity in the mantle. Chem. Geol. 376, 20–30.
Harvey, J., Savov, I.P., Agostini, S., Cliff, R.A., Walshaw, R., 2014b. Si-metasomatism in serpentinized peridotite: the effects of talc-alteration on strontium and boron isotopes in abyssal serpentinites from Hole 1268a, ODP Leg 209. Geochim. Cosmochim. Acta 126, 30–48. https://doi.org/10.1016/j.gca.2013.10.035.
Hasui, Y., Abreu, F.A.M., Silva, J.M.R., 1977. Estratigrafia da faixa de dobramentos Paraguai-Araguaia no centro-norte do Brasil. Bol. IG 8, 107–117.
Hodel, F., et al., 2019. A Neoproterozoic hyper-extended margin associated with Rodinia's demise and Gondwana's build-up: The Araguaia Belt, central Brazil. Gondwana Res. 66, 43–62. https://doi.org/10.1016/j.gr.2018.08.010.
Ishizuka, O., Kimura, J., Li, Y., Stern, R., Reagan, M., Taylor, R., Ohara, Y., Bloomer, S., Ishii, T., Hargroveiii, U., 2006. Early stages in the evolution of Izu–Bonin arc volcanism: new age, chemical, and isotopic constraints. Earth Planet. Sci. Lett. 250, 385–401. https://doi.org/10.1016/j.epsl.2006.08.007.
Ishizuka, O., Yuasa, M., Tamura, Y., Shukuno, H., Stern, R.J., Naka, J., Joshima, M., Taylor, R.N., 2010. Migrating shoshonitic magmatism tracks Izu–Bonin–Mariana intra-oceanic arc rift propagation. Earth Planet. Sci. Lett. 294, 111–122. https://doi.org/10.1016/j.epsl.2010.03.016.
Jochum, K.P., Stoll, B., 2008. Reference materials for elemental and isotopic analyses by LA-(MC)-ICP-MS: successes and outstanding needs. In: Laser Ablation ICP-MS in the Earth Sciences: Current Practices and Outstanding Issues. Mineral. Assoc. Can, pp. 147–168.
Jochum, K.P., Wilson, S.A., Abouchami, W., Amini, M., Chmeleff, J., Eisenhauer, A., Hegner, E., Iaccheri, L.M., Kieffer, B., Krause, J., 2011. GSD-1G and MPI-DING reference glasses for in situ and bulk isotopic determination. Geostand. Geoanal. Res. 35, 193–226.
Kasemann, S., Meixner, A., Rocholl, A., Vennemann, T., Rosner, M., Schmitt, A.K., Wiedenbeck, M., 2001. Boron and oxygen isotope composition of certified reference materials NIST SRM 610/612 and reference materials JB-2 and JR-2. Geostand. Newslett. 25, 405–416.
Kimura, J.-I., Chang, Q., Ishikawa, T., Tsujimori, T., 2016. Influence of laser parameters on isotope fractionation and optimisation of lithium and boron isotope ratio measurements using laser ablation-multiple Faraday collector-inductively coupled plasma mass spectrometry. J. Anal. At. Spectrom. 31, 2305–2320.
Lécuyer, C., Grandjean, P., Reynard, B., Albarède, F., Telouk, P., 2002. 11B/10B analysis of geological materials by ICP–MS Plasma 54: application to the boron fractionation between brachiopod calcite and seawater. Chem. Geol. 186, 45–55. https://doi.org/10.1016/S0009-2541(01)00425-9.
Li, Z.-X.A., Lee, C.-T.A., 2006. Geochemical investigation of serpentinized oceanic lithospheric mantle in the Feather River Ophiolite, California: implications for the recycling rate of water by subduction. Chem. Geol. 235, 161–185. https://doi.org/10.1016/j.chemgeo.2006.06.011.
Martin, C., Ponzevera, E., Harlow, G., 2015. *In situ* lithium and boron isotope determinations in mica, pyroxene, and serpentine by LA-MC-ICP-MS. Chem. Geol. 412, 107–116. https://doi.org/10.1016/j.chemgeo.2015.07.022.
Martin, C., Flores, K.E., Harlow, G.E., 2016. Boron isotopic discrimination for subduction-related serpentinites. Geology 44, 899–902.
Martin, C., Flores, K.E., Vitale-Brovarone, A., Angiboust, S., Harlow, G.E., 2020. Deep mantle serpentinization in subduction zones: insight from *in situ* B isotopes in slab and mantle wedge serpentinites. Chem. Geol. 545, 119637 https://doi.org/10.1016/j.chemgeo.2020.119637.
Mcculloch, M., Gregory, R., Wasserburg, G., Taylorjr, H., 1980. A neodymium, strontium, and oxygen isotopic study of the Cretaceous Samail ophiolite and implications for the petrogenesis and seawater-hydrothermal alteration of oceanic crust. Earth Planet. Sci. Lett. 46, 201–211. https://doi.org/10.1016/0012-821X(80)90006-0.
Metcalf, R.V., Shervais, J.W., 2008. Suprasubduction-zone ophiolites: is there really an ophiolite conundrum? Special Paper of the Geological Society of America 438, 191–222. https://doi.org/10.1130/2008.2438(07).
Mével, C., 2003. Serpentinization of abyssal peridotites at mid-ocean ridges. Comptes Rendus Geosci. 335, 825–852.
Miyashiro, A., 1973. The Troodos ophiolitic complex was probably formed in an island arc. Earth Planet. Sci. Lett. 19, 218–224. https://doi.org/10.1016/0012-821X(73)90118-0.
Moores, E.M., 1982. Origin and emplacement of ophiolites. Rev. Geophys. 20, 735. https://doi.org/10.1029/RG020i004p00735.
Moura, C.A., Gaudette, H.E., 1993. Zircon Ages of the Basement Ortho Gneisses of the Araguaia Belt, North-Central Brazil.
Orberger, B., Metrich, N., Mosbah, M., Mével, C., Fouquet, Y., 1999. Nuclear microprobe analysis of serpentine from the mid-Atlantic ridge. Nucl. Inst. Methods Phys. Res. B: Beam Interact. Mater. Atoms 158 (1–4), 575–581.
Pabst, S., Zack, T., Savov, I.P., Ludwig, T., Rost, D., Tonarini, S., Vicenzi, E.P., 2012. The fate of subducted oceanic slabs in the shallow mantle: insights from boron isotopes and light element composition of metasomatized blueschists from the Mariana forearc. Lithos 132–133, 162–179. https://doi.org/10.1016/j.lithos.2011.11.010.
Paixão, M.A.P., Nilson, A.A., Dantas, E.L., 2008. The Neoproterozoic Quatipuru ophiolite and the Araguaia fold belt, central-northern Brazil, compared with correlatives in NW Africa. In: Geol. Soc. London, Spec. Publ, p. 294.
Peacock, S.M., Hervig, R.L., 1999. Boron isotopic composition of subduction-zone metamorphic rocks. Chem. Geol. 160, 281–290. https://doi.org/10.1016/S0009-2541(99)00103-5.
Pearce, J.A., 2003. Supra-subduction zone ophiolites: The search for modern analogues. Special Paper of the Geological Society of America, 2003, 373, C. 2, 269-293.
Pearce, J.A., Reagan, M.K., 2019. Identification, classification, and interpretation of boninites from Anthropocene to Eoarchean using Si-Mg-Ti systematics. Geosphere 15, 1008–1037. https://doi.org/10.1130/GES01661.1.
Pearce, J.A., Lippard, S.J., Roberts, S., 1984. Characteristics and tectonic significance of supra-subduction zone ophiolites. Geol. Soc. Spec. Publ. 16, 77–94. https://doi.org/10.1144/GSL.SP.1984.016.01.06.
Penrose Conference, 1972. Ophiolites. Geotimes 17, 24–25.
Picazo, S., Müntener, O., Manatschal, G., Bauville, A., Karner, G., Johnson, C., 2016. Mapping the nature of mantle domains in Western and Central Europe based on clinopyroxene and spinel chemistry: evidence for mantle modification during an extensional cycle. Lithos 266, 233–263.
Prigent, C., Guillot, S., Agard, P., Ildefonse, B., 2018. Fluid-assisted deformation and strain localization in the cooling mantle wedge of a young subduction zone (Semail Ophiolite). J. Geophys. Res. Solid Earth 123, 7529–7549.
Pubellier, M., Monnier, C., Maury, R., Tamayo, R., 2004. Plate kinematics, origin and tectonic emplacement of supra-subduction ophiolites in SE Asia. Tectonophysics 392, 9–36. https://doi.org/10.1016/j.tecto.2004.04.028.
Roumejon, S., Früh-Green, G.L., Orcutt, B.N., the IODP Expedition 357 Science Party, 2018a. Alteration heterogeneities in peridotites exhumed on the southern wall of the Atlantis Massif (IODP Expedition 357). J. Petrol. 59, 1329–1358. https://doi.org/10.1093/petrology/egy065.
Roumejon, S., Williams, M.J., Früh-Green, G.L., 2018b. In-situ oxygen isotope analyses in serpentine minerals: constraints on serpentinization during tectonic exhumation at slow- and ultraslow-spreading ridges. Lithos 323, 156–173. https://doi.org/10.1016/j.lithos.2018.09.021.
Scambelluri, M., Tonarini, S., 2012. Boron isotope evidence for shallow fluid transfer across subduction zones by serpentinized mantle. Geology 40, 907–910.
Spivack, A., Edmond, J., 1987. Boron isotope exchange between seawater and the oceanic crust. Geochim. Cosmochim. Acta 51, 1033–1043.
Steinmann, G., 1927. Der ophiolitischen Zonen in der mediterranean Kettengebirgen. In: Presented at the 14th International Geological Congress, Madrid, pp. 638–667.
Stern, R.J., Reagan, M., Ishizuka, O., Ohara, Y., Whattam, S., 2012. To understand subduction initiation, study forearc crust: to understand forearc crust, study ophiolites. Lithosphere 4, 469–483. https://doi.org/10.1130/L183.1.
Stosch, H.-G., 1981. Sc, Cr, Co and Ni partitioning between minerals from spinel peridotite xenoliths. Contrib. Mineral. Petrol. 78, 166–174. https://doi.org/10.1007/BF00373778.
Tirrul, R., Bell, I.R., Griffis, R.J., Camp, V.E., 1983. The Sistan suture zone of eastern Iran. Geol. Soc. Am. Bull. 94, 134. https://doi.org/10.1130/0016-7606(1983)94<134:TSSZOE>2.0.CO;2.
Tsujimori, T., Sisson, V.B., Liou, J.G., Harlow, G.E., Sorensen, S.S., 2006. Very-low-temperature record of the subduction process: a review of worldwide lawsonite eclogites. Lithos 92, 609–624.
Vils, F., Tonarini, S., Kalt, A., Seitz, H.-M., 2009. Boron, lithium and strontium isotopes as tracers of seawater–serpentinite interaction at Mid-Atlantic ridge, ODP Leg 209. Earth Planet. Sci. Lett. 286, 414–425. https://doi.org/10.1016/j.epsl.2009.07.005.
Viti, C., Mellini, M., 1998. Mesh textures and bastites in the Elba retrograde serpentinites. Eur. J. Mineral. 10, 1341–1360. https://doi.org/10.1127/ejm/10/6/1341.
Wakabayashi, J., Dilek, Y., 2004. What constitutes "emplacement" of an ophiolite?: Mechanisms and relationship to subduction initiation and formation of metamorphic soles. Geol. Soc. Spec. Publ. 218, 427–447. https://doi.org/10.1144/GSL.SP.2003.218.01.22.
Whitney, D.L., Evans, B.W., 2010. Abbreviations for names of rock-forming minerals. Am. Miner. 95, 185.
Wunder, B., Meixner, A., Romer, R.L., Wirth, R., Heinrich, W., 2005. The geochemical cycle of boron: constraints from boron isotope partitioning experiments between mica and fluid. Lithos 84, 206–216. https://doi.org/10.1016/j.lithos.2005.02.003.
Yamada, C., Tsujimori, T., Chang, Q., Kimura, J., 2019a. Boron isotope compositions of antigorite–grade serpentinites in the Itoigawa–Omi area of the Hida–Gaien Belt, Japan. J. Mineral. Petrol. Sci. 114, 290–295. https://doi.org/10.2465/jmps.190726.
Yamada, C., Tsujimori, T., Chang, Q., Kimura, J.-I., 2019b. Boron isotope variations of Franciscan serpentinites, northern California. Lithos 334, 180–189.
Zhu, G., Ma, J., Wei, G., Zhang, L., 2021. Boron mass fractions and δ^{11} B values of eighteen international geological reference materials. Geostand. Geoanal. Res. 45, 583–598. https://doi.org/10.1111/ggr.12397.